

---

This is an electronic reprint of the original article.  
This reprint may differ from the original in pagination and typographic detail.

Rawlings, Alexander; Keitaanranta, Atte; Mattero, Max; Soininen, Sonja; Wright, Ruby J.; Kallioinen, Noa; Liao, Shihong; Rantala, Antti; Johansson, Peter H.; Naab, Thorsten; Irodoutou, Dimitrios

## Identifying supermassive black hole recoil in elliptical galaxies

*Published in:*  
Monthly Notices of the Royal Astronomical Society

*DOI:*  
[10.1093/mnras/staf238](https://doi.org/10.1093/mnras/staf238)

Published: 01/03/2025

*Document Version*  
Publisher's PDF, also known as Version of record

*Published under the following license:*  
CC BY

*Please cite the original version:*  
Rawlings, A., Keitaanranta, A., Mattero, M., Soininen, S., Wright, R. J., Kallioinen, N., Liao, S., Rantala, A., Johansson, P. H., Naab, T., & Irodoutou, D. (2025). Identifying supermassive black hole recoil in elliptical galaxies. *Monthly Notices of the Royal Astronomical Society*, 537(4), 3421-3447.  
<https://doi.org/10.1093/mnras/staf238>

---

This material is protected by copyright and other intellectual property rights, and duplication or sale of all or part of any of the repository collections is not permitted, except that material may be duplicated by you for your research use or educational purposes in electronic or print form. You must obtain permission for any other use. Electronic or print copies may not be offered, whether for sale or otherwise to anyone who is not an authorised user.

# Identifying supermassive black hole recoil in elliptical galaxies

Alexander Rawlings<sup>1</sup>,<sup>1</sup>★ Atte Keitaanranta,<sup>1</sup> Max Mattero,<sup>1</sup> Sonja Soinen,<sup>1</sup> Ruby J. Wright<sup>1,2</sup>,<sup>1,2</sup>  
 Noa Kallioinen,<sup>3</sup> Shihong Liao<sup>4</sup>,<sup>4</sup> Antti Rantala<sup>5</sup>,<sup>5</sup> Peter H. Johansson<sup>6</sup>,<sup>1</sup> Thorsten Naab<sup>5</sup>  
 and Dimitrios Irodotou<sup>6</sup>

<sup>1</sup>Department of Physics, University of Helsinki, Gustaf Hällströmin katu 2, FI-00014 Helsinki, Finland

<sup>2</sup>International Centre for Radio Astronomy Research (ICRAR), University of Western Australia, Crawley, WA 6009, Australia

<sup>3</sup>Department of Computer Science, Aalto University, Konemiehentie 2, FI-02150 Espoo, Finland

<sup>4</sup>Key Laboratory for Computational Astrophysics, National Astronomical Observatories, Chinese Academy of Sciences, Beijing 100101, China

<sup>5</sup>Max-Planck-Institut für Astrophysik, Karl-Schwarzschild-Str 1, D-85748 Garching, Germany

<sup>6</sup>The Institute of Cancer Research, 123 Old Brompton Road, London SW7 3RP, UK

Accepted 2025 February 5. Received 2025 January 22; in original form 2024 October 18

## ABSTRACT

We study stellar core growth in simulations of merging massive ( $M_{\star} > 10^{11} M_{\odot}$ ) elliptical galaxies by a supermassive black hole (SMBH) displaced by gravitational wave induced recoil velocity. With controlled, dense sampling of the SMBH recoil velocity, we find the core radius originally formed by SMBH binary scouring can grow by a factor of 2–3 when the recoil velocity exceeds  $\sim 50$  per cent of the central escape velocity, and the mass deficit grows by up to a factor of  $\sim 4$ . Using Bayesian inference we predict the distribution of stellar core sizes formed through this process to peak at  $\sim 1$  kpc. An orbital decomposition of stellar particles within the core reveals that radial orbits dominate over tube orbits when the recoil velocity exceeds the velocity dispersion of the core, whereas tube orbits dominate for the lowest recoil kicks. A change in orbital structure is reflected in the anisotropy parameter, with a central tangential bias present only for recoil velocities less than the local stellar velocity dispersion. Emulating current integral field unit observations of the stellar line-of-sight velocity distribution, we uncover a distinct signature in the Gauss–Hermite symmetric deviation coefficient  $h_4$  that uniquely constrains the core size due to binary scouring. This signature is insensitive to the later evolution of the stellar mass distribution due to SMBH recoil. Our results provide a novel method to estimate the SMBH recoil magnitude from observations of local elliptical galaxies, and implies these galaxies primarily experienced recoil velocities less than the stellar velocity dispersion of the core.

**Key words:** black hole physics – methods: numerical – software: simulations – galaxies: kinematics and dynamics.

## 1 INTRODUCTION

Observations have revealed a clear bimodality in the properties of massive elliptical galaxies, with brighter ellipticals ( $M_B \lesssim -20.5$ ) typically having ‘cored’ flat central surface brightness profiles, boxy isophotes, and showing little or no rotation (slow rotators). Fainter intermediate-mass ellipticals ( $-20.5 \lesssim M_B \lesssim -18.5$ ), on the other hand, typically show steeper ‘cuspy’ central brightness profiles, more disc-like isophotes and evidence for more rotational support (fast rotators) (e.g. Kormendy & Bender 1996; Faber et al. 1997; Emsellem et al. 2007; Kormendy et al. 2009; Dullo & Graham 2014; Thomas et al. 2014; Dullo 2019; Quenneville et al. 2024).

The observed bimodality can be linked to the distinct formation paths of elliptical galaxies. Intermediate-mass ellipticals have likely formed predominantly through in-situ star formation and in mergers of gas-rich disc-dominated galaxies accompanied by merger-induced starbursts resulting in cuspy central stellar profiles (e.g. Barnes & Hernquist 1996; Cappellari et al. 2007; Johansson, Naab & Burkert

2009; Hopkins et al. 2009a, b; Krajnović et al. 2011; Cappellari 2016; Lahén et al. 2018; Förster Schreiber & Wuyts 2020). More massive elliptical galaxies are, on the other hand, believed to have assembled in a two-stage process, in which the early assembly at redshifts of  $z \gtrsim 1.5$  is dominated by in-situ star formation fuelled by cold gas flows in massive dark matter (DM) haloes, and the accretion of multiple star-bursting progenitors. The later evolution of the galaxies then proceeds mainly through gas-poor (dry) merging in which the galaxy predominantly accretes stars formed outside the main galaxy (e.g. Bezanson et al. 2009; Naab, Johansson & Ostriker 2009; Oser et al. 2010; Johansson, Naab & Ostriker 2012; Wellons et al. 2015; Rodriguez-Gomez et al. 2016; Qu et al. 2017; Lagos et al. 2022; Cannarozzo et al. 2023, see also Naab & Ostriker 2017 for a review). However, if massive galaxies have formed by merging of fainter cuspy galaxies they should also possess central cusps, as simulations have shown that mergers tend to preserve the density cusps of merging galaxies (Boylan-Kolchin, Ma & Quataert 2004; Dehnen 2005).

In the case of two massive elliptical galaxies undergoing a dry merger, the leading mechanism for stellar core formation is through the interaction of binary supermassive black holes (SMBHs) in

\* E-mail: [alexander.rawlings@helsinki.fi](mailto:alexander.rawlings@helsinki.fi)

the galaxy merger remnant. The merging of SMBHs is generally understood in the context of a three-stage process (Begelman, Blandford & Rees 1980). First, the dynamical friction from the mass overdensity in the wakes of the SMBHs provides a restoring force which brings the SMBHs to the centre of the two interacting galaxies (Chandrasekhar 1943), generally torquing the SMBHs to highly radial orbits in the process. Secondly, after the mass enclosed within the orbit of the two SMBHs is comparable to the sum of the SMBH masses, the SMBHs form a bound binary (Merritt & Milosavljević 2005). Iterative interactions of the SMBHs with surrounding stars on low angular momentum orbits (the stellar ‘loss-cone’ population) eject these stars with high velocity (e.g. Hills & Fullerton 1980; Hills 1983; Quinlan 1996), thus removing orbital energy and angular momentum from the SMBH binary orbit. The removal of stars from the central regions by this slingshot mechanism produces a ‘core’ (e.g. Lauer 1983; Kormendy 1984; Lauer 1985), or depletion, in the luminosity profile of the remnant galaxy (e.g. Begelman et al. 1980; Hills 1983; Quinlan 1996; Rantala et al. 2018; Nasim et al. 2021; Khonji et al. 2024; Partmann et al. 2024; Rantala et al. 2024), which can in extreme cases extend up to 3 kpc (Postman et al. 2012). Early numerical simulations found that during the scouring of the stellar core, the loss-cone population of stars can be exhausted if the galactic nucleus has a high degree of spherical symmetry, thus preventing the SMBH binary from reaching separations below roughly one parsec. This phenomenon is termed the final-parsec problem (Milosavljević & Merritt 2001). Subsequent work found that, in the gas-free case, stellar orbit diffusion from more realistic triaxial potentials prevents the loss-cone from emptying, allowing the SMBH binary to reach sub-parsec separations (e.g. Berczik et al. 2006; Holley-Bockelmann & Sigurdsson 2006; Merritt & Vasiliev 2011; Vasiliev, Antonini & Merritt 2015; Gualandris et al. 2017). At these very small separations the SMBH binary loses its remaining orbital energy and angular momentum through gravitational wave (GW) emission, driving the SMBH binary to coalescence (Peters & Mathews 1963; Peters 1964). The GW emission from such SMBH coalescence events are prime observational targets for ongoing pulsar timing array (PTA) detectors for SMBHs with masses of  $M_{\bullet} \gtrsim 10^9 M_{\odot}$  (Agazie et al. 2023; Xu et al. 2023; Zic et al. 2023; EPTA Collaboration 2024), and also the forthcoming *Laser Interferometer Space Antenna (LISA)* mission for SMBHs with slightly lower masses of  $M_{\bullet} \lesssim 10^8 M_{\odot}$  (Amaro-Seoane et al. 2023).

The final GW emission from the coalescing SMBH binary occurs anisotropically, and carries with it linear momentum from the system (e.g. González et al. 2007a). This results in the remnant SMBH recoiling with some velocity directed opposite to the linear momentum of the GW emission (Bekenstein 1973), and is termed the kick, or recoil, velocity.<sup>1</sup> The kick velocity is dependent on the mass ratio between the SMBHs prior to coalescence, and the magnitude and direction of the angular momentum (spin) vector of each SMBH. As reported by Campanelli et al. (2007), symmetries in the masses or spins of the SMBHs suppresses the resulting recoil kick imparted to the coalesced SMBH. In particular, it is found that asymmetry in the spins of the SMBHs has a larger impact on the magnitude of the recoil kick than asymmetry in the masses (Campanelli et al. 2007), with spins which are anti-aligned in the orbital plane and maximal producing the largest recoil kick velocities (González et al. 2007b; Tichy & Marronetti 2007). Numerical relativity studies indicate that while the majority of recoil kicks are of the order of a few hundred

kilometres per second, in special configurations the SMBH may be imparted a kick velocity in excess of  $2000 \text{ km s}^{-1}$ , even up to  $4000 \text{ km s}^{-1}$  (Campanelli et al. 2007; González et al. 2007b; Tichy & Marronetti 2007). Taking the central escape velocity of a typical massive elliptical galaxy as  $\sim 2000 \text{ km s}^{-1}$ , there may be a non-negligible fraction of elliptical galaxies with an SMBH that has escaped the galaxy (e.g. Madau & Quataert 2004; Mannerkoski et al. 2022), though not so many so as to introduce considerable scatter into the observed relation between SMBH mass and stellar velocity dispersion (Volonteri 2007).

Numerous observational studies have also hinted at the existence of recoiling SMBHs, generally through either an offset from the centre of the host galaxy in velocity, in position, or both. One of the earliest observations that pointed to a recoiling SMBH was of the quasar SDSSJ0927+2943, reported by Komossa, Zhou & Lu (2008), where an observed velocity offset suggested a recoil kick in excess of  $2600 \text{ km s}^{-1}$ . Another recoiling SMBH candidate was identified by an offset in velocity by Steinhardt et al. (2012), with an estimated recoil velocity greater than  $4000 \text{ km s}^{-1}$ . Other observations by Comerford & Greene (2014) and Pesce et al. (2018, 2021) have also reported potential recoiling SMBHs, albeit at much lower kick velocities (some tens to few hundreds of  $\text{km s}^{-1}$ ). Recoiling SMBHs may also be identified through a spatial offset from the host centre, where the offset can range from some parsecs (Batcheldor et al. 2010; Lena et al. 2014; Barrows et al. 2016) to over a kiloparsec (Koss et al. 2014; Skipper & Browne 2018). Additionally, some candidate recoiling SMBHs have both spatial and velocity offsets, such as CXO J101527.2+625911 (Kim et al. 2017) and 2MASX J00423991+3017515 (Hogg et al. 2021). Attributing an escaping SMBH to GW recoil as opposed to three-body interactions between an SMBH binary and a third SMBH is also not trivial, as demonstrated in the recent observations presented in van Dokkum et al. (2023).

Numerically, the effect of recoiling SMBHs on the formation of cores in massive elliptical galaxies has been primarily studied using collisionless simulations. Early work by Boylan-Kolchin et al. (2004) found that a recoiling SMBH induced a core in the stellar density profile, particularly when the SMBH remained bound to the bulge of the host galaxy and had a recoil velocity comparable to the bulge velocity dispersion. In another early study Merritt et al. (2004) also found that recoiling SMBHs facilitated the formation of cores and found that ejected SMBHs settled roughly in one orbital period in spherical potentials, with this ‘infall time’ increasing when more realistic triaxial potentials were considered. In Gualandris & Merritt (2008) the motion of a settling SMBH in a stellar potential representative of a galaxy merger remnant was found to occur in three stages: first, the SMBH oscillates with decreasing amplitude due to energy dissipation by dynamical friction. Next, both the SMBH and stellar core oscillate about their common centre of mass when the radial excursion of the SMBH is less than the core radius of the stellar system. Finally, the SMBH settles into thermal equilibrium with the surrounding stars. During these three stages, the stellar density core is enhanced by the motion of the SMBH, producing a mass deficit in some cases up to five times the SMBH mass (see also Boylan-Kolchin et al. 2004; Merritt et al. 2004; Partmann et al. 2024). However, a recent study by Nasim et al. (2021) on the contribution to stellar core expansion through GW recoil of an SMBH found intriguingly that the greatest contribution to the stellar mass deficit is due to the first excursion of the SMBH following its ejection, with subsequent oscillations only providing a minor contribution to the growth of the stellar core.

<sup>1</sup>We use the terms ‘kick’ and ‘recoil’ interchangeably in this work.

Whilst previous studies have convincingly shown that there is a clear case for a relation between SMBH recoil velocity and the final core size carved out by its motion, little attention has been devoted to understanding the statistical impact of SMBH recoil on the properties of the merger remnant galaxy, for example the distribution of core sizes that result from realistic SMBH recoil velocities. Work by Nasim et al. (2021) and Khonji et al. (2024) considered specific examples of local massive ETGs, invoking large SMBH recoil velocities with up to 90 per cent of the galaxy escape velocity as a mechanism to grow the most massive observed cores. These works also considered varying SMBH masses and stellar density profiles, affecting the contribution to core growth by SMBH binary scouring. Whilst successful in explaining extreme core sizes, such high recoil velocities are unlikely to be the norm, given that all observed elliptical galaxies host a central SMBH (Ferrarese et al. 1994; Häring & Rix 2004; Kormendy & Ho 2013; van den Bosch 2016). The role of more typical SMBH recoil velocities (of the order a few to several hundred kilometres per second, e.g. Campanelli et al. 2007) in core formation in general, and not just in the case of the most massive cores, remains largely unexplored. In addition, how a recoiling SMBH impacts the surrounding stellar orbital distribution has remained largely unanswered. Orbital modelling techniques, in particular orbit-superposition Schwarzschild modelling, offer a unique bridging between observations and simulations, often revealing a rich understanding of a galaxy’s history, and the effect of SMBH interactions (e.g. Röttgers, Naab & Oser 2014; Neureiter et al. 2021; Santucci et al. 2022; Neureiter et al. 2023; Santucci et al. 2023, 2024).

In this study, we use the GADGET-4 based regularized tree code KETJU (Rantala et al. 2017, 2020; Mannerkoski et al. 2023) to study the effect of recoiling SMBHs on the structure of massive elliptical galaxies. Previously, KETJU has been used to study the formation of cores through SMBH binary scouring in gas-free simulations, but without the contribution of SMBH recoils (Rantala et al. 2018, 2019, 2024). Here, we run a large set of gas-free simulations with systematically varying SMBH kick velocities. The aim of this work is twofold. We first aim to determine how the velocity with which the SMBH is kicked affects the mass distribution of the surrounding stellar environment, and the likelihood of the magnitude of these effects. We then aim to determine if a recoiling SMBH imparts a signature on the stellar kinematics of the remnant galaxy, and if such a signature could potentially be observed with current detectors.

This paper is divided as follows: we present the numerical simulations used in our investigation in Section 2. We discuss the motion of the recoiling SMBHs in Section 3, and the resulting stellar density profiles of the remnant galaxy in Section 4. We investigate the distribution of stellar orbits as a function of the kick velocity in Section 5 and construct mock stellar kinematic observations to be compared with observational data in Section 6. Finally, we discuss our results in Section 7 and present our conclusions in Section 8, respectively.

## 2 NUMERICAL SIMULATIONS

### 2.1 Simulation code

To investigate the effect of the recoiling SMBH on the host galaxy, and potential observational signatures of this, we run a number of numerical simulations of an idealized galaxy merger setting using

the new public version of the KETJU<sup>2</sup> code (Rantala et al. 2017, 2020; Mannerkoski et al. 2023) coupled with GADGET-4 (Springel et al. 2021). KETJU integrates the dynamics of SMBHs, and stellar particles in a small region three times the stellar softening length around them (i.e. the KETJU region), to high accuracy using the algorithmically regularized integrator MSTAR (Rantala et al. 2020). The dynamics of stellar particles beyond this small region of high integration accuracy, and all DM particles, is computed with the GADGET-4 fast multiple method (FMM) with second-order multipoles. Additionally, we use hierarchical time integration, which allows for mutually symmetric interactions and manifest momentum conservation. In this study, we do not use comoving integration, as we are investigating an idealized system. KETJU also includes post-Newtonian (PN) correction terms up to order 3.5 between each pair of SMBHs (Blanchet 2014) and the fitting formula of Zlochower & Lousto (2015) for recoil kick velocity, making KETJU a particularly well-suited code for investigating the consequence of SMBH recoil self-consistently in a galaxy merger environment.

### 2.2 Initial conditions

We model the merger of two massive elliptical galaxies using gas-free merger simulations. Our galaxy initial conditions follow that of IC  $\gamma$ -1.0-BH-6 presented in Rantala et al. (2018) but scaled down by a factor of  $\sim 3$  in mass, consistent with the method presented in Rantala et al. (2019). As we are interested in the evolution of the galaxy merger *remnant* following SMBH coalescence, the initial conditions are constructed such that at the time of SMBH coalescence (Section 2.3) the galaxy remnant agrees with local scaling relations. Specifically, we ensure that our remnant agrees with the half-light-stellar mass data presented in Sahu, Graham & Davis (2020), and lies within the  $1\sigma$  prediction interval of the SMBH mass–stellar velocity dispersion data as given in den Bosch (2016).

The galaxy is represented as an isotropic multicomponent sphere, and consists of a stellar component of total mass  $M_\star \sim 1.38 \times 10^{11} M_\odot$  embedded within a DM component of total mass  $M_{\text{DM}} = 2.5 \times 10^{13} M_\odot$ . At the centre an SMBH with mass  $M_{\bullet,0} = 2.93 \times 10^9 M_\odot$  is placed with zero velocity. The stellar and DM components each follow a Hernquist (1990) profile with a scale radius of  $a_\star = 3.9$  kpc and  $a_{\text{DM}} = 245$  kpc, respectively. The density profile  $\rho_i$  for a given component  $i$  is given by:

$$\rho_i(r) = \frac{M_i}{2\pi} \frac{a_i}{r(r+a_i)^3}. \quad (1)$$

We generate the ICs using the distribution function method following Hiltz et al. (2012) and Rantala et al. (2017), where for each component (stellar and DM) the distribution function  $f_i$  is computed using Eddington’s formula (Binney & Tremaine 2008) for each density profile  $\rho_i$ :

$$f_i(\mathcal{E}) = \frac{1}{2\sqrt{2}\pi^2} \int_{\Phi_T=0}^{\Phi_T=\mathcal{E}} \frac{d^2\rho_i}{d\Phi_T^2} \frac{d\Phi_T}{\sqrt{\mathcal{E}-\Phi_T}}. \quad (2)$$

Here  $\mathcal{E}$  is the relative energy, and  $\Phi_T$  is the total gravitational potential. The distribution functions are then sampled with discrete particles, where the mass of a stellar particle is set to  $m_\star = 5 \times 10^4 M_\odot$ , and the mass of a DM particle is set to  $m_{\text{DM}} = 5 \times 10^6 M_\odot$ . The radial velocity profiles of both stellar and DM particles are ergodic.

<sup>2</sup><https://www.mv.helsinki.fi/home/phjohans/group-website/research/ketju/>

### 2.3 Merger simulations

We merge two independently Monte Carlo sampled galaxy ICs, creating an equal-mass galaxy merger with a near-radial orbit. The merger orbit has an initial separation consistent with Rantala et al. (2018) of  $D = 30$  kpc, however the initial eccentricity is set to  $e_0 = 0.97$ , and the first pericentre distance adjusted accordingly to  $r_{\text{peri}} = D(1 - e_0^2) \simeq 2$  kpc (Khochfar & Burkert 2006; Rantala et al. 2017). The merger configuration results in a rapid coalescence of the SMBH binary, however we note that the merger time-scale we observe is driven by stochasticity in the binary eccentricity (Nasim et al. 2020; Rawlings et al. 2023). The resulting coalesced SMBH has a mass  $M_{\bullet} = 2M_{\bullet,0} = 5.86 \times 10^9 M_{\odot}$ . We then select the snapshot just prior ( $\sim 8$  Myr) to the GW-driven SMBH merger, and generate 31 ‘child’ simulations, where each child has a unique gravitational recoil kick velocity  $v_{\text{kick}}$  prescribed along the  $x$ -axis,<sup>3</sup> ranging from 0 to  $1800 \text{ km s}^{-1}$  (inclusive), in  $60 \text{ km s}^{-1}$  increments. The upper limit on  $v_{\text{kick}}$  is chosen to match the escape velocity of the centre of the merger remnant,  $v_{\text{esc}} = 1800 \text{ km s}^{-1}$ . We additionally run one simulation with a recoil kick above  $v_{\text{esc}}$ , with  $v_{\text{kick}} = 2000 \text{ km s}^{-1}$ , to test the effect of rapidly removing an SMBH.

For all simulations, snapshots are produced every 5 Myr. Interactions between stellar particles are softened with a softening length of  $\varepsilon_{\star} = 2.5$  pc following Rawlings et al. (2023), DM is softened with a softening length of  $\varepsilon_{\text{DM}} = 300$  pc, and the KETJU region radius is set to  $r_{\text{ketju}} = 3\varepsilon_{\star} = 7.5$  pc to ensure that the stellar–SMBH interactions are always non-softened (Rantala et al. 2017). Within the KETJU region, dynamical interactions between stellar particles and SMBHs, and SMBHs–SMBHs are unsoftened. For the GADGET-4 component of the simulation, the integration error tolerance is set to 0.002, whereas the Gragg–Bulirsch–Stoer (GBS) tolerance for KETJU is set to  $10^{-8}$ .

We impose a maximum integration time on all simulations, corresponding to three dynamical times  $t_{\text{dyn}}$ , defined in terms of the virial radius  $r_{200}$  and virial velocity  $v_{200}$  of the galaxy merger remnant as:

$$t_{\text{dyn}} = \frac{r_{200}}{v_{200}} \simeq 1 \text{ Gyr.} \quad (3)$$

Thus, our simulations are run for a maximum of 3 Gyr.

## 3 SETTling SMBHS

### 3.1 Motion of the kicked SMBH

Before the SMBH binary coalescence, the binary scours a stellar core with a radius of  $r_{\text{b},0} \sim 0.58$  kpc in the centre of the galaxy (see Section 4.2). In the interior of the core, the stellar 1D velocity dispersion is  $\sigma_{\star,0} \equiv \sigma_{\star}(r < r_{\text{b},0}) \sim 270 \text{ km s}^{-1}$ . Immediately following the coalescence of the SMBH binary and the subsequent kick, the trajectory of the remnant SMBH is predominantly radial in the direction of the GW recoil kick, as shown in Fig. 1. We can thus estimate the crossing time of the binary-scoured core based on the 1D stellar velocity dispersion as:

$$t_{\text{cross,core}} \simeq \frac{r_{\text{b},0}}{\sigma_{\star,0}} \approx 2 \text{ Myr,} \quad (4)$$

<sup>3</sup>As the  $x$ -axis is in the global coordinate frame, the direction of the kick is essentially random with respect to the angular momentum and inertia tensors. To test the effect of differing kick directions on the merger remnant, we test directing the recoil kick along the global  $y$ -axis, and find very similar evolution to the  $x$ -axis case.

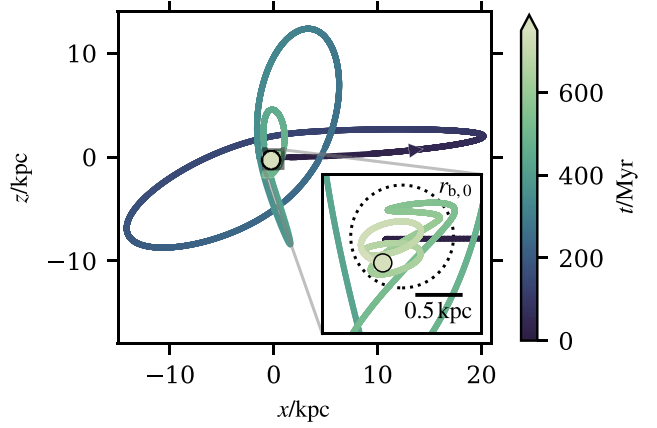


**Figure 1.** The trajectory of the kicked SMBH in the  $v_{\text{kick}} = 780 \text{ km s}^{-1}$  simulation, with its final position shown by the marked circle. The line is coloured by the time following merger, and an arrow displays the initial outward radial motion of the SMBH for clarity. The inset panel depicts the motion of the SMBH as it is settling within the binary-scoured core radius, marked by the dotted circle. The final settling of the SMBH is chaotic once its velocity falls below the local stellar velocity dispersion: it is unable to leave the core again from this moment onwards.

whereas the actual time the recoiling SMBH traverses the core is:

$$t_{\text{cross},\bullet} \simeq \frac{r_{\text{b},0}}{v_{\text{kick}}}. \quad (5)$$

If the velocity of the recoil kick is not high enough to completely eject the SMBH from the galaxy ( $v_{\text{kick}} < v_{\text{esc}}$ ), the SMBH will oscillate about the centre of the galaxy. The amplitude of the oscillations, termed the apocentre distance  $r_{\text{apo}}$ , decreases with each oscillation due to dynamical friction, which is automatically resolved with KETJU (e.g. Karl et al. 2015; Rantala et al. 2017; Genina, Springel & Rantala 2024). Ultimately the SMBH ‘settles’ to the centre of the galaxy. If  $v_{\text{kick}} < \sigma_{\star,0}$ , the SMBH has insufficient kinetic energy to escape the stellar core and instead remains within 100 pc from the centre, shown in the top panel of Fig. 2. Conversely, if  $v_{\text{kick}} > \sigma_{\star,0}$  the SMBH can exit the core, with  $r_{\text{apo}}$  increasing as  $v_{\text{kick}}$  is increased. If  $r_{\text{apo}}$  exceeds  $\sim 10$  kpc, mild triaxiality in the outer regions of the galaxy merger remnant (shown in Fig. A1) can torque the SMBH into an orbit with some degree of tangential motion, an example of which is given in Fig. 1 for the  $v_{\text{kick}} = 780 \text{ km s}^{-1}$  simulation. For the first few orbits, the SMBH may thus not necessarily pass through the stellar core, though it loses energy to the surrounding medium with each oscillation. During the final passages however, the SMBH passes through the core, before its velocity decreases below the velocity dispersion of the core. The predominantly radial motion of the SMBH rapidly degrades to a random walk as it settles to the Brownian limit from this point, and does not leave the core again (shown in the inset panel of Fig. 1).

### 3.2 Identifying a settled SMBH

As we focus on galaxy merger remnants and the possible observational signatures caused by recoil kicks in this work, we analyse herein times after the SMBH has settled back to the centre of the galaxy. Therefore we first need to determine the time (the infall time henceforth) where this occurs. The stellar centre of the merger remnant is found using the shrinking sphere method (Power et al. 2003): we use this method herein for our analysis. We begin by estimating the expected Brownian velocity of an SMBH

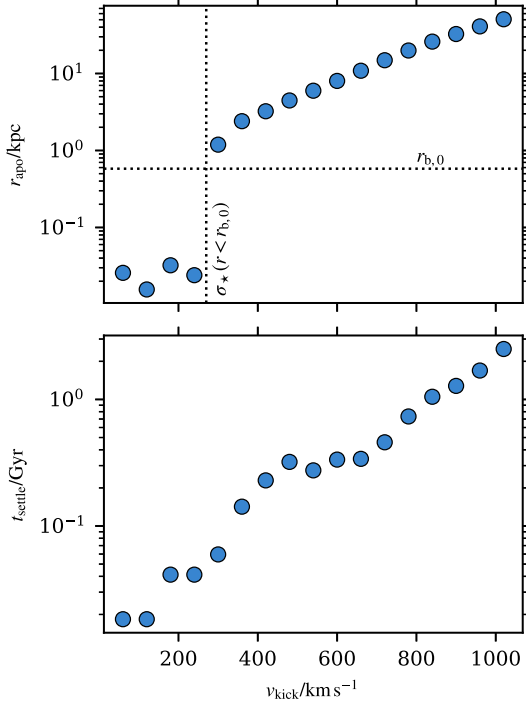


**Figure 2.** Top panel: the distance of the first apocentre passage from the centre of the galaxy for each kick velocity that resulted in a settled SMBH. The horizontal dashed line,  $r_{b,0}$ , marks the size of the stellar core the SMBH binary scours before coalescence, and the vertical dashed line,  $\sigma_*(r < r_{b,0})$ , is the 1D velocity dispersion of the stellar particles interior to the binary-scoured core radius. Bottom panel: the settling times for each kick velocity with  $v_{\text{kick}} > 0 \text{ km s}^{-1}$ . The time increases exponentially as  $v_{\text{kick}}$  increases.

in a distribution of stellar and DM particles of lower unit mass ( $m_*, m_{\text{DM}} \ll M_*$ ) following Merritt, Berczik & Laun (2007). We determine the root-mean-square velocity of the massive particle as

$$V_{\text{RMS}} = \sqrt{3\xi\bar{\sigma}}, \quad (6)$$

where  $\bar{\sigma}$  is the average velocity dispersion of the stellar and DM particles, and  $\xi$  is the mass ratio to the SMBH, calculated as:

$$\xi = \frac{\int n(m)m^2 dm}{\int n(m)m dm} / M_*, \quad (7)$$

where  $n(m)$  is the number density of particles with masses  $m$  to  $m + dm$ . Our calculated value of  $V_{\text{RMS}}$  that we use to define a settled velocity is  $V_{\text{RMS}} \sim 25 \text{ km s}^{-1}$ .

Next, we go through the simulations output in ‘windows’ of 100 Myr. If the SMBH stays within 0.1 kpc from the centre and has a median velocity less than  $V_{\text{RMS}}$  relative to the centre within the 100 Myr window, we consider the SMBH to be settled at the time when the velocity first falls below  $V_{\text{RMS}}$  within the time interval. The chosen separation from the centre is smaller than the large offsets observed by Barrows et al. (2016) and slightly larger than the  $\lesssim 10 \text{ pc}$  offsets in Lena et al. (2014).

The settling times are shown in the lower panel of Fig. 2. For recoil velocities  $v_{\text{kick}} \leq 240 \text{ km s}^{-1}$  the kick is not large enough to displace the SMBH beyond the binary-scoured core and the SMBH is considered settled in less than 100 Myr after SMBH binary coalescence. As the kick velocity is increased further, the settling time begins to increase exponentially. The slight deviations from an

exponential increase are caused by numerical noise, which prevents the median velocity being below  $V_{\text{RMS}}$ .

The SMBHs which received a kick velocity larger than  $1020 \text{ km s}^{-1}$  did not settle back to the centre of the galaxy within the maximum simulation time of  $3t_{\text{dyn}} = 3 \text{ Gyr}$ , and already reach maximum displacements in excess of  $> 60 \text{ kpc}$  during their first excursion from the centre. We expect that any SMBH with such a large displacement from its host galaxy would not be observationally identified with that galaxy, and thus we do not include simulations with  $v_{\text{kick}} > 1020 \text{ km s}^{-1}$  in this analysis. The used limit for maximum displacement is a few times larger than the largest suggested offset of 19.4 kpc from observations (Barrows et al. 2016). We do however analyse the  $v_{\text{kick}} = 2000 \text{ km s}^{-1}$  simulation, which is above the escape velocity of the galaxy, as a proxy for an SMBH that is almost instantaneously removed from the simulation. Importantly, an escaping SMBH never completes a single oscillation about the centre of the galaxy.

### 3.3 Movement of stellar mass by a settling SMBH

We consider the amount of stellar mass that is bound to the recoiling SMBH,  $M_{*,\text{bound}}$ , at different times following coalescence. A stellar particle is defined to be bound to the SMBH if it is within the influence radius  $r_{\text{infl}}$  of the SMBH, which satisfies (e.g. Merritt 2013):

$$M_*(r < r_{\text{infl}}) = 2M_*. \quad (8)$$

and the binding energy of the stellar particle  $K - U$ , where  $K$  is the kinetic energy and  $U$  is the potential energy (in the SMBH frame of reference), is less than zero. We determine the SMBH influence radius to be  $r_{\text{infl}} \simeq 1.5 \text{ kpc}$  at the time of SMBH coalescence. At each pericentre passage of the oscillating SMBH (where the SMBH velocity is maximal),  $M_{*,\text{bound}}$  is minimal; conversely,  $M_{*,\text{bound}}$  is maximal at apocentre, irrespective of  $v_{\text{kick}}$ . Increasing  $v_{\text{kick}}$  however reduces the magnitude of  $M_{*,\text{bound}}$  compared to lower values of  $v_{\text{kick}}$ . Following coalescence for the  $v_{\text{kick}} = 60 \text{ km s}^{-1}$  case (the lowest, non-zero recoil velocity simulated),  $M_{*,\text{bound}} \sim 2.18 \times 10^9 M_{\odot}$ , or roughly 37 per cent of the coalesced SMBH mass and less than 2 per cent of the total stellar mass. By  $v_{\text{kick}} = 1020 \text{ km s}^{-1}$ ,  $M_{*,\text{bound}}$  has decreased to 0.2 per cent of the coalesced SMBH mass. These results are in close quantitative agreement with the findings of Gualandris & Merritt (2008) and agree well with those of Nasim et al. (2021), despite different initial conditions being used between our study and those in the literature. We hypothesize that the movement of stellar mass bound to the SMBH is not the dominant mechanism by which the stellar mass distribution changes, and investigate this further in Section 4.3.

The core region of the galaxy constantly evolves while the SMBH moves through the galaxy. We inspect how the Lagrangian radius relative to the centre of mass and enclosing a stellar mass equal to the SMBH mass,  $r(M_* = M_*)$ , evolves with time in Fig. 3 until the SMBH is settled. In addition to kick velocities  $v_{\text{kick}} \leq 1020 \text{ km s}^{-1}$ , the kick velocity  $v_{\text{kick}} = 2000 \text{ km s}^{-1}$  is included. As the SMBH with  $v_{\text{kick}} = 2000 \text{ km s}^{-1}$  is completely removed from the galaxy and does not settle back to the centre, the evolution is shown for  $\sim 2.0 \text{ Gyr}$  following SMBH binary coalescence.

During the first  $\sim 30 \text{ Myr}$ , the initial evolution of the Lagrangian radii is very similar for kick velocities  $v_{\text{kick}} > 300 \text{ km s}^{-1}$ . We can understand this from the core-crossing time argument, where if

$$\frac{v_{\text{kick}}}{\sigma_{*,0}} > 1 \Rightarrow \frac{t_{\text{cross},*}}{t_{\text{cross,core}}} < 1. \quad (9)$$

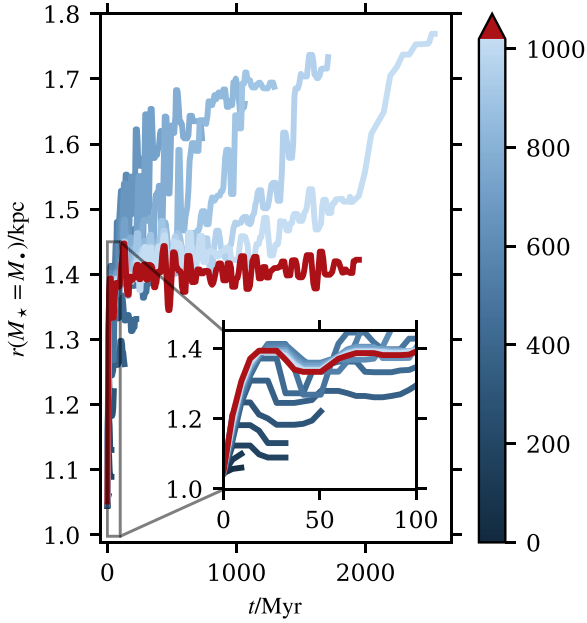


**Figure 3.** The radius from the centre of the galaxy which encloses a stellar mass equivalent to the mass of the SMBH as a function of time for each kick velocity. Recoil velocities from 0 to 1020  $\text{km s}^{-1}$  are shown with a continuous colour scale, and the 2000  $\text{km s}^{-1}$  simulation is shown in red. For each recoil velocity, the Lagrangian radius is shown until the SMBH has settled. The evolution is shown until  $t \sim 2.0$  Gyr for the SMBH ejected from the galaxy with a 2000  $\text{km s}^{-1}$  kick. During the first  $\sim 30$  Myr, the Lagrangian radius increases with larger kick velocities resulting in larger growth of the core. For the kick velocities that manage to generate multiple oscillations from the centre, the Lagrangian radius increases further when the SMBH travels through the core region during its final few orbits.

Consequently, for  $v_{\text{kick}} > \sigma_{*,0}$ , the SMBH is moving faster than the stellar core is able to react to the rapid change in potential caused by the recoiling SMBH. For these simulations, the Lagrangian radii initially increases sharply to  $\sim 1.4$  kpc and the SMBH leaves the core almost instantly. This large rise occurs during the first oscillation. The trend which the Lagrangian radius follows at this phase is caused by the reaction of the core region to the changed gravitational potential (Boylan-Kolchin et al. 2004). Each simulation shifts away from the trend when the SMBH returns to the centre. For  $v_{\text{kick}} < \sigma_{*,0}$ , the SMBH settles back to within 100 pc from the centre before the Lagrangian radius can reach  $\sim 1.4$  kpc.

The higher recoil kick velocities in Fig. 3 show that the Lagrangian radii can further increase at later times in addition to the initial increase, as long as the SMBH is kicked beyond the core. The increase is larger for higher kick velocities, with the Lagrangian radius in the simulation with  $v_{\text{kick}} = 1020 \text{ km s}^{-1}$  reaching nearly 1.8 kpc. As was seen from Fig. 1, the SMBH can miss the core region entirely during the first few orbits. The Lagrangian radius is only affected when the SMBH passes through the core, or very near to it. For each of the simulations with  $\sigma_{*,0} < v_{\text{kick}} \leq 1020 \text{ km s}^{-1}$ , the final few orbits will always include a passage through the core region. The SMBHs which received larger kick velocities possess more kinetic energy compared to those SMBHs which received smaller kick velocities and will cross the core region more times. Since the SMBH struggles to leave the core region during the final oscillations, the kinetic energy heats up the stellar particles within the central region, causing the additional growth of the Lagrangian radius.

Importantly, the Lagrangian radius for each  $v_{\text{kick}}$  stays largely constant for times after  $t_{\text{settle}}$ . Thus, the core region of the galaxy has had enough time to react to the effect the kicked SMBH has caused at the moment when the SMBH settles at the centre. Based on this, the state of the galaxy merger remnant at  $t = t_{\text{settle}}$  captures the full effect which the kicked SMBH has on the galaxy.

### 3.4 Relaxation time

As already discussed, the time required for the kicked SMBH to return and settle at the centre of the merger remnant in general increases with increasing recoil velocity. To ensure that our results are robust to the variable ending time of the simulations, and are not a manifestation of relaxation processes, we determine the relaxation time of the  $v_{\text{kick}} = 0 \text{ km s}^{-1}$  system at different radii. We conservatively estimate the relaxation time  $t_{\text{relax}}$  at a radius  $r$  as (Binney & Tremaine 2008):

$$t_{\text{relax}} \simeq 2.1 \frac{\sigma r^2}{G\bar{m} \ln \Lambda}, \quad (10)$$

where  $\sigma$  is the particle velocity dispersion within  $r$ ,  $\bar{m}$  is the mean particle mass (hence the mean of the stellar and DM particle masses), and  $\Lambda$  is the argument of the Coulomb logarithm, given by:

$$\Lambda = \frac{r \langle v^2 \rangle}{2G\bar{m}}, \quad (11)$$

where  $\langle v^2 \rangle$  is the mean-squared particle velocity within  $r$ . The relaxation time increases quadratically with increasing  $r$ , and we find for a radius of  $r = 1.0$  kpc the relaxation time to be  $t_{\text{relax}} \sim 5.0$  Gyr; this increases to  $\sim 100$  Gyr by  $r = 5$  kpc. Of the simulations where the SMBH was determined to have settled, the maximum time for this to occur was  $\sim 2.5$  Gyr, well below the relaxation time of the system. We note that equation (10) does not take into account gravitational softening, and thus provides a conservative lower bound for the relaxation time. This is critical as the KETJU region does not include gravitational softening between stellar particles and the SMBH, so it is not a fully softened simulation. In practice, we expect the relaxation time to be even longer than reported due to the inclusion of gravitational softening in the simulation for particles outside of the KETJU region. Thus, for the analysis herein, we are confident that the results we observe are directly caused by the influence of the recoiling SMBH on the galaxy, and are not due to relaxation effects.

## 4 STELLAR MASS DENSITY PROFILES

### 4.1 3D mass density profiles

Before considering the projected, 2D stellar mass density profiles of the merger remnants, we investigate the 3D stellar mass distribution. This alleviates the influence of projection effects on inferring if a core has formed during the SMBH binary merger process, and gives insight into the dependence of how matter is spatially distributed as a function of the recoiling SMBH kick velocity.

In Fig. 4, we observe a clear decrease in stellar mass density at radii  $r \lesssim 2$  kpc with increasing kick velocity. For  $v_{\text{kick}} = 0 \text{ km s}^{-1}$ , the central stellar density is  $\sim 10^{10} \text{ M}_{\odot} \text{ kpc}^{-3}$ , whereas for  $v_{\text{kick}} = 1020 \text{ km s}^{-1}$  it is  $\sim 10^9 \text{ M}_{\odot} \text{ kpc}^{-3}$ . An exception to this trend is the highest kick velocity we simulated,  $v_{\text{kick}} = 2000 \text{ km s}^{-1}$ , which shows an excess of stellar mass between  $0.3 \lesssim r/\text{kpc} \lesssim 2$  relative to the simulations with  $v_{\text{kick}} \gtrsim 300 \text{ km s}^{-1}$ . This is readily explained by the evolution of the Lagrangian radii in Fig. 3. The final few orbits of the settling SMBH in simulations with  $v_{\text{kick}} > 300 \text{ km s}^{-1}$  take

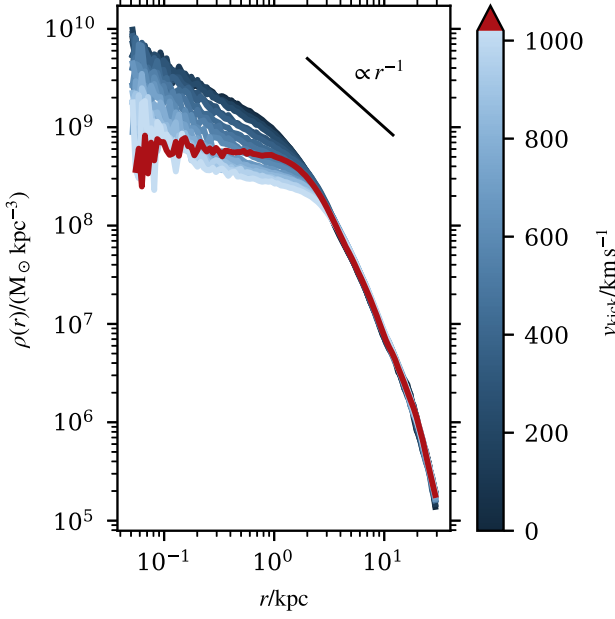


**Figure 4.** 3D stellar mass density, with the line colour corresponding to the kick velocity of the SMBH. At radii  $r \lesssim 3$  kpc, the stellar mass density decreases smoothly with increasing kick velocity, with the exception of the  $v_{\text{kick}} = 2000 \text{ km s}^{-1}$  simulation, in which the SMBH has not returned to the centre of the merger remnant. A density cusp is apparent for all mergers where the SMBH settled at the centre. At radii  $r > 2$  kpc all the density profiles are consistent with each other, indicating that a changing SMBH recoil velocity has a larger impact on the inner mass distribution of the galaxy merger remnant.

the SMBH through the stellar core, enlarging it further with each oscillation. As a result, the central stellar density decreases as the number of oscillations increase. The  $v_{\text{kick}} = 2000 \text{ km s}^{-1}$  simulation, in which the SMBH does not oscillate through the core, has a central stellar density that decreases only due to the initial response of the stellar particles to the sudden change of the potential. The simulations with a settled SMBH have a density profile within  $r < 1$  kpc that follows a power law  $\rho \propto r^{-\nu}$  with  $0 < \nu < 1$ . Conversely, the  $v_{\text{kick}} = 2000 \text{ km s}^{-1}$  simulation has a flat density profile with  $\nu = 0$  in the centre, in agreement with the recent work by Khonji et al. (2024).

In the outer regions  $r \gtrsim 4$  kpc, the stellar density falls with increasing radius consistently between all simulations, indicating that the dynamical effect of a recoiling SMBH on the stellar mass distribution is predominantly confined to the central regions of the galaxy.

## 4.2 Projected mass density profiles

To facilitate comparisons with observations (e.g. Graham et al. 2003; Rusli et al. 2013), we fit the six-parameter core-Sérsic profile (Graham et al. 2003) to the projected stellar mass density of each simulated merger remnant:

$$\Sigma(R) = \Sigma' \left[ 1 + \left( \frac{r_b}{R} \right)^\alpha \right]^{\gamma/\alpha} \exp \left[ -b_n \left( \frac{R^\alpha + r_b^\alpha}{R_e^\alpha} \right)^{(1/\alpha n)} \right], \quad (12)$$

where

$$\Sigma' = \Sigma_b 2^{-\gamma/\alpha} \exp \left[ b_n \left( 2^{1/\alpha} \frac{r_b}{R_e} \right)^{1/n} \right]. \quad (13)$$

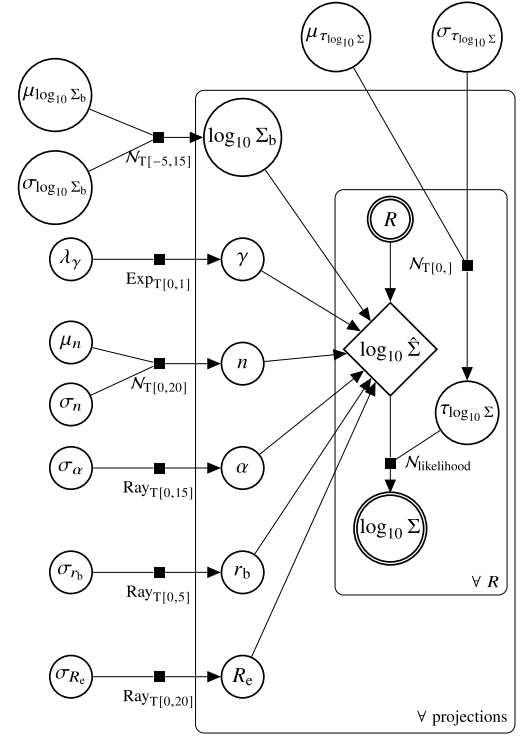


**Figure 5.** Directed acyclic graph of the core-Sérsic model of projected mass density within the Bayesian hierarchical framework. Single-line circle nodes represent fit parameters, double-line circles represent measured quantities (the data), and diamond nodes represent deterministic quantities. The particular distribution connecting nodes is written below the corresponding black square, with a subscript ‘ $T[l, u]$ ’ denoting a distribution  $f(\lambda)$  truncated to  $l < \lambda < u$ , and the subscript ‘likelihood’ indicating the likelihood function. The  $R$  box indicates variables fit for each radial bin, and the projection box distinguishes variables specific to each projection realization. Note that we additionally use  $\hat{\Sigma}$  to distinguish the calculated value of surface density from the measured value  $\Sigma$ . The various distributions are normal ( $\mathcal{N}$ ), exponential (Exp), and Rayleigh (Ray).

Here  $r_b$  is the core radius,  $\Sigma_b$  is the projected surface density at the core radius,  $\gamma$  is the core slope,  $R_e$  is the effective (half-light) radius,<sup>4</sup>  $n$  is the Sérsic index,  $b_n$  is estimated as  $b_n \simeq 2n - 1/3 + 0.009876/n$  (Prugniel & Simien 1997), and  $\alpha$  is the profile transition index. We refer to the collective vector of these parameters as  $\theta \equiv [r_b, \Sigma_b, \gamma, R_e, n, \alpha]$ . We view the simulated merger remnant from  $N_{\text{proj}} = 15$  random angles in  $N_R = 21$  logarithmically spaced bins from 0.1 to 30 kpc, and use a Bayesian hierarchical model to fit the model parameters, as shown in Fig. 5, with the hyperparameter distributions given in Table 1. An excellent introduction to Bayesian data analysis, and in particular the strengths of hierarchical modelling in encoding dependencies between model parameters without overfitting, can be found in Gelman et al. (2015), which we summarize in Section B of the Appendix in the context of our work. As part of the Bayesian inference workflow, we perform rigorous prior sensitivity analysis and posterior checking, also detailed in Section B of the Appendix.

<sup>4</sup>As we assume a constant mass-to-light ratio, the half-light radius is equivalent to the projected half-mass radius.



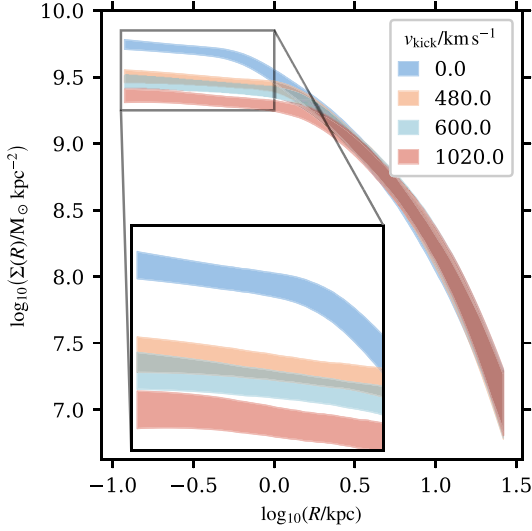


**Figure 6.** Surface density profiles with 25 per cent Bayesian HDI for select representative runs. Increasing the kick velocity induces a shallower density profile in the inner regions, consistent with the 3D density maps in Fig. 4.

In Fig. 6, we see a clear decrease in the projected stellar mass density with increasing kick velocity for four representative values of  $v_{\text{kick}}$ , consistent with the results in Fig. 4. The shaded regions in Fig. 6 correspond to the 25 per cent Bayesian highest density interval (HDI), where the uncertainty is a direct result of choosing different projection angles when constructing the projected densities.

To discuss the difference in the evacuated core region of the merger remnants more quantitatively, we show the median (blue dashes) and interquartile range (IQR, blue boxes) of the core radius parameter  $r_b$  from equation (12) for kick velocities  $v_{\text{kick}} \leq 1020 \text{ km s}^{-1}$  in Fig. 7, in units of both kpc and scaled to the  $v_{\text{kick}} = 0 \text{ km s}^{-1}$  core radius  $r_{b,0}$ , which corresponds to the pre-merger core radius of the galaxy. Our results indicate that a non-zero kick velocity where the SMBH returns to the centre of the merger remnant serves to enlarge the core region relative to the core formed during the SMBH binary scouring phase. In agreement with previous studies, we find a monotonic increase in the core radius  $r_b$  with kick velocity. Additionally, we see that the IQR of  $r_b$  increases with increasing  $v_{\text{kick}}$ , indicating that with an increased core size, the uncertainty introduced due to projection effects also increases. To test the significance of the difference in distributions of  $r_b$  between the  $v_{\text{kick}} = 0 \text{ km s}^{-1}$  case and the  $v_{\text{kick}} = 1020 \text{ km s}^{-1}$  case, we calculate the probability of superiority (PS, Grissom & Kim 2001) as:

$$\text{PS} = \frac{1}{n} \sum_i \mathbb{1}_{r_{b,0}^{(i)} < r_{b,1020}^{(i)}}(i), \quad (14)$$

where the index  $i$  runs over the  $n$  posterior samples, and the indicator function  $\mathbb{1}_A$  maps the  $i$ -th posterior draw to 1 if it belongs to the subset  $A$ , and to 0 otherwise. With this measure we find that in more than 87 per cent of the posterior draws,  $r_b$  from the  $v_{\text{kick}} = 1020 \text{ km s}^{-1}$  case is greater than  $r_b$  from the  $v_{\text{kick}} = 0 \text{ km s}^{-1}$  case; the distributions are distinct.

As shown in the top right panel of Fig. B1 in the Appendix, the projected density at the core radius decreases with increasing kick velocity, in agreement with the decreasing core density observed in the 3D density profiles in Fig. 4. Similarly, the Sérsic index  $n$  also decreases with increasing kick velocity (bottom right panel of Fig. B1). For recoil velocities  $v_{\text{kick}} \leq 300 \text{ km s}^{-1}$ ,  $n \simeq 2.1$ , and

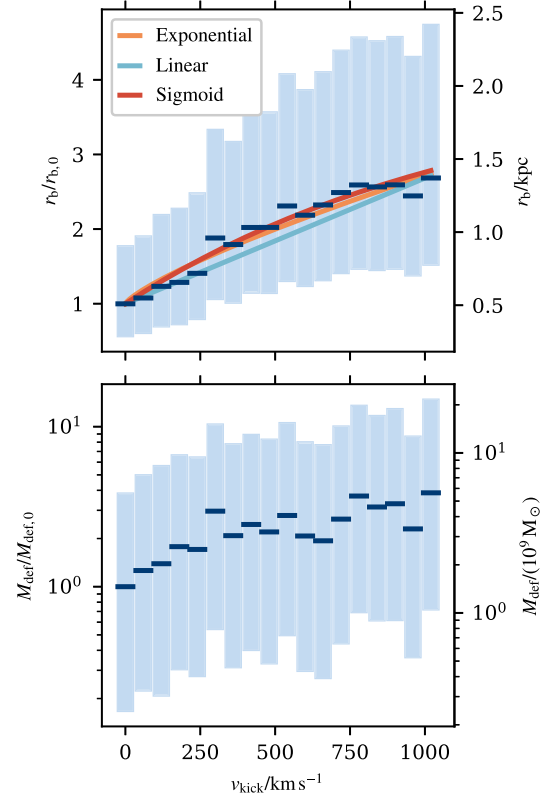


**Figure 7.** Top panel: Bayesian estimate of the merger remnant core size  $r_b$ , scaled to the core size scoured solely by the SMBH binary prior to coalescence  $r_{b,0}$  (left axis) and in physical units (right axis), as a function of kick velocity  $v_{\text{kick}}$ . The core size distributions are shown as box plots, with the median core size indicated by the central mark and shaded regions corresponding to the IQR. Larger kick velocities are correlated with larger core sizes. Additionally, a greater spread in the distribution of core sizes over different viewing projections of the merger remnant is associated with larger kick velocities. Three models, fit to the median  $r_b$ - $v_{\text{kick}}$  trend, are overplotted. For the models, we do not show the parameter uncertainty for visual clarity. Bottom panel: Box plots of the Monte Carlo sampled mass deficit  $M_{\text{def}}$  between Sérsic and core-Sérsic fits as a function of the recoil velocity.  $M_{\text{def}}$  is scaled to the mass deficit due to SMBH binary scouring ( $M_{\text{def},0}$ , left axis) and shown in physical units (right axis).

for  $v_{\text{kick}} \geq 660 \text{ km s}^{-1}$ ,  $n \simeq 1.6$ . For recoil velocities  $360 \text{ km s}^{-1} \leq v_{\text{kick}} \leq 600 \text{ km s}^{-1}$ , the decrease in  $n$  appears linear. We note that the recoil velocity for which  $n$  begins to decrease coincides closely with the stellar velocity dispersion of the SMBH binary-scoured core,  $\sigma_{*,0} \sim 270 \text{ km s}^{-1}$ . The variation in  $n$  can be understood in the context of the SMBH leaving the core, and thus affecting the stellar mass distribution beyond the core as it oscillates back to its equilibrium state. Conversely, the effective radius  $R_e$  appears insensitive to the SMBH recoil velocity.

For the inner slope parameter  $\gamma$ , a weak trend to lower values at higher recoil velocities is apparent, after peaking at  $v_{\text{kick}} \sim 300 \text{ km s}^{-1} \sim \sigma_{*,0}$ , though the distributions for  $\gamma$  are broad. Recently, Khonji et al. (2024) demonstrated that increasing SMBH recoil velocity resulted in a suppressed  $\gamma$ , however the authors did not capture the  $v_{\text{kick}} \sim \sigma_{*,0}$  regime of recoil velocities. We understand the broad distributions that we observe for  $\gamma$  as arising from the collapse of a 3D density distribution to a 2D representation, and then enforcing a spherically symmetric 1D profile to describe the 2D surface density. This is supported by the IQR of the  $\gamma$  parameter

remaining relatively broad with irrespective of kick velocity, unlike the core radius  $r_b$  for example.

To investigate this further, for a subset of simulations we take particles in the centre of the merger remnant within a spherical annulus defined by  $0.9 \text{ kpc} \leq r \leq 1.0 \text{ kpc}$  and consider sixty different, random projections into the 2D plane. We perform a singular value decomposition (SVD) to obtain an ellipse representation of the projected annulus, and determine the ellipticity  $\varepsilon$  of the projection

$$\varepsilon = \frac{a - b}{a}, \quad (15)$$

where  $a$  and  $b$  are the semimajor and semiminor axes of the ellipse, respectively. A value of  $\varepsilon \neq 0$  indicates a departure from circular symmetry. We find the distribution of  $\varepsilon$  is positively constrained and peaks at  $\varepsilon \simeq 0$  but is right-skewed, with the 75-th percentile of  $\varepsilon$  typically about  $\sim 0.05$ . This indicates that asymmetries are present in the projected stellar mass density profiles. Non-circularity of the core region complicates using a radially parametrized density profile parametrized by a constant exponent  $\gamma$ : a range of possible values for  $\gamma$  could describe the core region comparatively well. The difficulty in constraining  $\gamma$  provides good motivation for determining distributions for the parameters in equation (12) with Bayesian techniques, as opposed to point estimates achieved through typical frequentist methods.

### 4.3 Estimating the amount of missing stellar mass

We continue the quantitative analysis of the core region by calculating the missing stellar mass of the merger remnants. As well as the core radius  $r_b$ , the mass deficit  $M_{\text{def}}$  can also be used to measure the core size. Past studies have found the mass deficit to correlate with the combined mass of the SMBH binary and the number of major ‘dry’ mergers (e.g. Milosavljević & Merritt 2001; Graham et al. 2003; Merritt 2006; Rantala et al. 2024). In order to determine the mass displaced by the gravitational interactions and recoil, we adopt an observational approach by comparing the stellar mass density profiles of the inward extrapolated Sérsic  $\Sigma_s(R)$  (Sérsic 1963, 1968) and the core-Sérsic  $\Sigma(R)$  fits (e.g. Dullo & Graham 2014; Bonfini & Graham 2016; Dullo 2019; Nasim et al. 2021) as:

$$M_{\text{def}} = 2\pi \int_0^\infty [\Sigma_s(R) - \Sigma(R)] R dR, \quad (16)$$

assuming a constant mass-to-light ratio (Bonfini & Graham 2016). The core-Sérsic profile is calculated using equations (12) and (13), while the Sérsic profile can be obtained using the same set of equations with a slight modification. By setting  $r_b = 0$  in equation (12), the profile becomes the standard Sérsic profile:

$$\Sigma_s = \Sigma' \exp\left(-b_n \left(\frac{R}{R_e}\right)^{1/n}\right). \quad (17)$$

To achieve the right normalization, it is important to let  $r_b$  retain its value in equation (13) when constructing the Sérsic profile (Graham et al. 2003). In fitting the luminosity profiles, we perform for each kick velocity  $10^4$  Monte Carlo samplings of the posterior distributions of the parameters  $\theta \equiv [r_b, \Sigma_b, \gamma, R_e, n, \alpha]$  described earlier in Section 4.2, hence giving us  $10^4$  realizations of the quantity  $M_{\text{def}}$ .

The resulting mass deficits as a function of kick velocities  $v_{\text{kick}} \leq 1020 \text{ km s}^{-1}$  are shown in the lower panel of Fig. 7. At low kick velocities,  $v_{\text{kick}} \leq 240 \text{ km s}^{-1}$ , we see a slow monotonic increase of mass deficit as a function of the kick velocity. Although the scatter grows at higher kick velocities, an increase of the median trend can

be observed over the whole kick velocity range. For high  $v_{\text{kick}}$  we see a median trend of  $M_{\text{def}} \sim 4M_{\text{def},0}$ , where  $M_{\text{def},0}$  corresponds to the mass deficit from binary scouring alone. We find that the median mass deficit due to SMBH binary scouring prior to the coalescence of the SMBHs is  $M_{\text{def},0} = 1.46 \times 10^9 M_\odot$ , roughly  $0.25M_\bullet$ . As a consequence of the mass deficit growing to  $M_{\text{def}} \sim M_\bullet$  for non-zero recoil velocities, as well as  $M_{\text{def}}$  correlating positively with recoil velocity, we confirm our earlier hypothesis in Section 3.3 that stellar mass bound to the SMBH (at most  $0.37M_\bullet$ ) is not the primary mechanism by which the core grows.

There are numerous ways to calculate the mass deficit in simulations, and differences between methods along with varying initial conditions may contribute to discrepancies across studies. A common approach to calculating the mass deficit, which we also adopt, is to compare the Sérsic and the extrapolated core-Sérsic profiles (Graham et al. 2003; Dosopoulou, Greene & Ma 2021; Nasim et al. 2021). This technique has been used by Dullo & Graham (2014) for observations of cored galaxies, resulting in typical mass deficits of  $0.5 \lesssim M_{\text{def}}/M_\bullet \lesssim 4$ ; these mass deficits may not be due solely to SMBH binary scouring however. Other methods, including calculating the difference in densities between the initial and final states of the galaxy merger (e.g. Merritt 2006; Gualandris & Merritt 2008), and running the simulations with and without SMBHs (e.g. Partmann et al. 2024; Rantala et al. 2024), typically find greater mass deficits than we do, but of the same magnitude.

As for core sizes presented in Fig. 7, the interquartile ranges of the missing mass broaden with increasing kick velocities. This is due to growing uncertainties in the projection effects, even though the parameters  $\theta$  from the core-Sérsic fits are Monte Carlo sampled as discussed at the end of Section 4.2. Also, we have found a positive correlation between mass deficit and the core radius. Thus, the increasingly large range of  $r_b$  values introduce a wider range of mass deficits as a function of kick velocity.

### 4.4 Predicted core size distribution

To predict the distribution of expected stellar core sizes given our merger remnant of two massive elliptical galaxies, we require a mapping from the kick velocity to the core radius. Let us define a scaled kick velocity  $v' = v_{\text{kick}}/v_{\text{esc}}$ . Previous work by Nasim et al. (2021) fit an empirical power law of the form:

$$\frac{r_b}{r_{b,0}} = K v'^q + 1, \quad (18)$$

where  $K$  and  $q$  are free parameters. Equation (18) gives that the core radius monotonically increases irrespective of kick velocity, naively implying that as  $v_{\text{kick}} \rightarrow \infty$ ,  $r_b \rightarrow \infty$ .

We test two other empirical relations between  $r_b$  and  $v_{\text{kick}}$ . The first is a simple linear relation:

$$\frac{r_b}{r_{b,0}} = K v' + 1, \quad (19)$$

and the second takes the form of a sigmoid function:

$$\frac{r_b}{r_{b,0}} = K \left(1 - e^{-qv'}\right) + 1. \quad (20)$$

We fit each of the exponential, linear, and sigmoid models to the median  $r_b$ - $v_{\text{kick}}$  trend in Fig. 7, and display the relation with its best-fitting parameters in the same figure. In the fit, we assume weakly informative positively constrained normally distributed priors on the parameters, a normally distributed scatter  $\tau$  truncated to  $\tau > 0$ , and a Gaussian likelihood function. The fit is found using the same Bayesian methods as in Section 4.2 (including posterior checking and

**Table 1.** Hyperparameter distributions for core-Sérsic model. The distributions are either a normal ( $\mathcal{N}$ ), exponential (Exp), or gamma (Gamma) distribution. The rationale for each distribution is discussed in Section B of the Appendix.

Hyperparameter	Distribution	Truncation
$\mu_{\log_{10} \Sigma_b}$	$\mathcal{N}(10, 2)$	None
$\sigma_{\log_{10} \Sigma_b}$	$\mathcal{N}(0, 1)$	$x > 0$
$\lambda_\gamma$	Exp(10)	None
$\mu_n$	$\mathcal{N}(8, 4)$	$0 < x \leq 15$
$\sigma_n$	$\mathcal{N}(0, 4)$	$x > 0$
$\sigma_\alpha$	Gamma(2, 0.2)	None
$\sigma_{r_b}$	$\mathcal{N}(0, 1)$	$x > 0$
$\sigma_{R_e}$	$\mathcal{N}(0, 12)$	$x > 0$
$\mu_{\tau_{\log_{10} \Sigma}}$	$\mathcal{N}(0, 1)$	$x > 0$
$\sigma_{\tau_{\log_{10} \Sigma}}$	$\mathcal{N}(0, 0.2)$	$x > 0$

**Table 2.** Values of the fitted parameters in the three core radius–kick velocity relations.

Model	Parameter	Median	68 per cent HDI
Exponential	$K$	2.72	[2.19, 3.34]
	$q$	0.78	[0.57, 0.99]
Linear	$K$	3.03	[2.39, 3.64]
Sigmoid	$K$	3.04	[1.66, 5.73]
	$q$	1.56	[0.51, 3.07]

prior sensitivity analysis), allowing for uncertainties to be estimated for the model fits. The medians and 68 per cent HDI interval of the relation parameters in equations (18)–(20) are given in Table 2.

Using the three  $r_b$ – $v_{\text{kick}}$  relations, we wish to construct the posterior predictive distributions for new data  $\tilde{r}_b$  given the observed values of  $r_b$ :

$$p(\tilde{r}_b | r_b) = \int p(\tilde{r}_b | \kappa) p(\kappa | r_b) d\kappa, \quad (21)$$

where the integral marginalizes out the respective  $r_b$ – $v_{\text{kick}}$  relation parameters, collectively referred to as  $\kappa$  (Gelman et al. 2015). To generate the new data  $\tilde{r}_b$ , we first generate a distribution of kick velocities for our merger configuration by randomly sampling SMBH spin values, as we assume this is the only unconstrained variable in our simulated SMBH merger. For the dimensionless SMBH spin parameter  $\alpha_\bullet$ , we use the distribution for dry mergers given in Zlochower & Lousto (2015), which takes the form of a beta distribution:

$$P_{\text{Zlochower}}(\alpha_\bullet) \propto (1 - \alpha_\bullet)^{4.66884 - 1} \alpha_\bullet^{10.5868 - 1} \quad (22)$$

and assume the direction of each SMBH spin vector is randomly distributed uniformly on the sphere. With the distribution of  $\alpha_\bullet$ , and the state of the SMBH binary just prior to coalescence, we use the relations presented in Zlochower & Lousto (2015) to obtain a distribution of SMBH recoil velocities.

The new data  $\tilde{r}_b$  is then generated by transformation sampling the distribution of kick velocities, and ‘pushing’ the values through the desired  $r_b$ – $v_{\text{kick}}$  relation. Using transformation sampling allows us to obtain a distribution of core radii predicted by a given kick velocity model, as shown in Fig. 8, whilst simultaneously accounting for uncertainty in the fit described by the  $r_b$ – $v_{\text{kick}}$  relations. Using  $10^4$  Monte Carlo sampled values for  $v_{\text{kick}}$ , where each value is used across

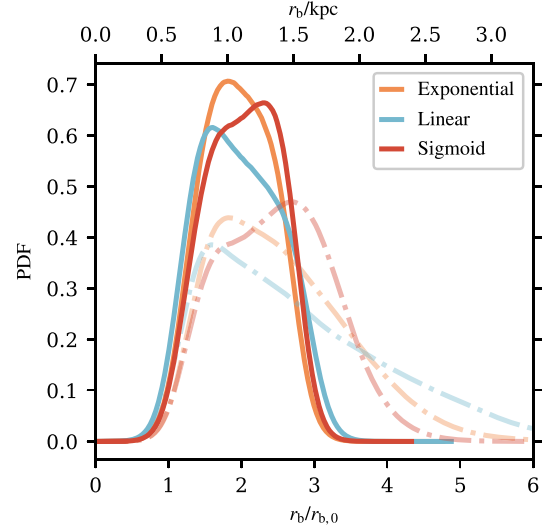


**Figure 8.** Probability density functions of transformation sampled core radii assuming a given model relation. Solid lines depict a truncated recoil velocity distribution, whereas dash-dot lines depict a non-truncated recoil velocity distribution. The SMBH spin vectors are Monte Carlo sampled from the Zlochower & Lousto (2015) relation assuming randomly aligned azimuthal spins to generate a distribution of recoil velocities, which are then pushed through each of the three fitted models in equations (18)–(20). The sigmoid model is the preferred model, and has its mode at a larger value of  $r_b$  than either the exponential or linear models, at  $r_b/r_{b,0} \sim 2.29$  ( $r_b/\text{kpc} \sim 1.27$ ) in the truncated case. The (non-truncated) predicted kick velocities range from  $v_{\text{kick}} = 0$  to  $v_{\text{kick}} \sim 4000 \text{ km s}^{-1}$ .

four chains each of length 2000 samples, provides a total sample size of  $8 \times 10^7$  values of  $\tilde{r}_b$ .

By only varying the SMBH spin vectors prior to merger, the range of kick velocities predicted by the model for the particular merger configuration in our study varies from  $v_{\text{kick}} = 0$  to  $v_{\text{kick,max}} \equiv v_{\text{kick}} \sim 4000 \text{ km s}^{-1}$ , with a peak at  $v_{\text{kick}} \simeq 250 \text{ km s}^{-1}$ . The maximum kick velocity that resulted in a settled SMBH in our sample,  $v_{\text{kick}} = 1020 \text{ km s}^{-1}$ , corresponds to the  $\sim 63$ rd percentile of the empirical cumulative distribution function (CDF) of the kick velocity distribution. Additionally, from the empirical CDF we find that approximately 10 per cent of recoil velocities exceed the escape velocity of the centre of the merger remnant,  $v_{\text{esc}} = 1800 \text{ km s}^{-1}$ .

The distribution of recoil velocities becomes slightly more right-skewed if the masses of the SMBHs are allowed to vary prior to merger. By randomly sampling each SMBH mass as  $M_{\bullet,\text{new}} = 10^{\mathcal{N}(0,0.3)} M_{\bullet,0}$ , where the dispersion of 0.3 is the intrinsic scatter in the  $M_\bullet$ – $M_{\text{bulge}}$  relation from Häring & Rix (2004), we find that a recoil velocity of  $1020 \text{ km s}^{-1}$  corresponds to the  $\sim 76$ th percentile, and the central escape velocity of  $v_{\text{esc}} = 1800 \text{ km s}^{-1}$  corresponds to the  $\sim 95$ th percentile. Thus, whilst a non-equal mass SMBH binary merger results in a slightly different recoil velocity distribution, large recoil velocities are still allowed, and are frequent, within the expected SMBH mass variation. Herein we consider our fiducial case of equal-mass SMBH binaries, but do not expect the conclusions to drastically differ in the more general case.

As we cannot be guaranteed that the proposed  $r_b$ – $v_{\text{kick}}$  relations hold beyond our fitted data range of  $0 \text{ km s}^{-1}$ – $1020 \text{ km s}^{-1}$ , we discuss the distribution of core radii in two parts: the first limiting our analysis to  $v_{\text{kick}} \leq 1020 \text{ km s}^{-1}$ , and the second to  $v_{\text{kick}} \leq v_{\text{kick,max}}$ .

#### 4.4.1 Core size distribution for $v_{\text{kick}} \leq 1020 \text{ km s}^{-1}$

To truncate the kick velocity distribution with an upper bound of  $1020 \text{ km s}^{-1}$ , we take only those values of  $v_{\text{kick}}$  which satisfy the velocity criterion, noting that as  $1020 \text{ km s}^{-1}$  corresponds to the  $\sim 63$ rd percentile, we still have in excess of  $4.5 \times 10^7$  samples of the core radius distribution.

We show the core radius distribution for the three different models with solid lines in Fig. 8. We find that the mode of the forward-folded core radius distribution is similar for the exponential and linear models, with  $1.01 \text{ kpc}$  ( $1.82 r_{\text{b},0}$ ) and  $0.88 \text{ kpc}$  ( $1.59 r_{\text{b},0}$ ), respectively. Conversely, the mode for the sigmoid relation occurs at a larger value of  $r_{\text{b}}$ , namely  $1.28 \text{ kpc}$  ( $2.31 r_{\text{b},0}$ ).

Looking at the shapes of the three distributions in Fig. 8, we see a similarity in shapes between the exponential and linear models, which are both slightly right-skewed. This is due to the ever-increasing value of  $r_{\text{b}}$  predicted for an increasing  $v_{\text{kick}}$ : higher recoil velocities produce larger cores, but as higher recoil velocities become increasingly unlikely (assuming the Zlochower & Lousto (2015) distribution), we observe the skew in the  $r_{\text{b}}$  probability density function (PDF). Conversely, the sigmoid model has a small hump prior to the mode, arising from the high likelihood of small kick velocities being pushed through the sigmoid function (equation 20) prior to the upper plateau of the function. The peak in the  $r_{\text{b}}$  distribution from the sigmoid model is a result of a large range of kick velocities (albeit with decreasing frequency) being mapped to the upper plateau of the sigmoid function, hence the correspondence between the median of the scale factor  $K = 3.04$  in equation (20) and the distribution mode for the model,  $2.31 r_{\text{b},0}$ .

To determine which model of the three (exponential, linear, or sigmoid) best describes the data, we use approximate leave-one-out cross-validation (LOO-CV) with Pareto smoothed importance sampling (PSIS; Vehtari, Gelman & Gabry 2017; Vehtari et al. 2024). PSIS LOO-CV estimates the expected log pointwise predictive density ( $\widehat{\text{ELPD}}$ ), defined

$$\widehat{\text{ELPD}} = \sum_{i=1}^N \log \int p(r_{\text{b},i} | \kappa) p(\kappa | r_{\text{b},-i}) d\kappa, \quad (23)$$

to determine the out-of-sample predictive accuracy of each model. The integral in equation (23) is analogous to equation (21), and gives the ability to predict the  $i$ -th data point  $r_{\text{b},i}$  when that same data point is excluded from the estimate of  $\kappa$ , namely  $p(\kappa | r_{\text{b},-i})$  (Gelman, Hwang & Vehtari 2014). A larger value of  $\widehat{\text{ELPD}}$  indicates better predictive ability of a given model compared to some other model (Vehtari et al. 2017; Riha et al. 2024). When performing the LOO-CV, we ensure that the Pareto- $k$  values in the PSIS method are below 0.5, indicating reliable importance sampling estimates (Vehtari et al. 2024).

We report the preferred model to be the sigmoid model (equation 20), with an  $\widehat{\text{ELPD}}$  of 1.70, compared to 1.58 and 0.61 for the exponential and linear models, respectively. However, we note that the difference in  $\widehat{\text{ELPD}}$  between the sigmoid and exponential models is not large, and the standard error of the difference in  $\widehat{\text{ELPD}}$ , denoted  $\widehat{\text{SE}}(\Delta \widehat{\text{ELPD}})$ , is 2.62 when comparing the sigmoid model to the exponential model, and 2.71 when comparing the sigmoid model to the linear model. This indicates that the difference between the models is likely not substantial in this range of recoil velocities.

#### 4.4.2 Core size distribution for $v_{\text{kick}} \leq v_{\text{kick,max}}$

We show the core radius distribution, without a truncation in the recoil velocity distribution, for the three different models with dash-dot lines in Fig. 8. For the exponential and linear models, the distributions of  $r_{\text{b}}$  are significantly right-skewed and broadened compared to when a truncation is applied to the recoil velocities. The right-skew arises due to the derivatives of these models being positive and greater than unity, resulting in increasingly higher recoil velocities being mapped to increasingly larger core radii. It is important to note that the mode of the  $r_{\text{b}}$  distributions for the exponential and linear models with and without recoil velocity truncation are consistent, despite the differing shape of the distributions. This is a result of low recoil velocities being more likely to occur, and hence contributing more to the transformation sampling of  $v_{\text{kick}}$  to  $r_{\text{b}}$ , than the high recoil velocity samples.

Similarly, the sigmoid model demonstrates a broader distribution of core radii when no truncation is applied to the recoil velocities compared to when a truncation is applied. However the overall shape is more consistent with the truncated case than in the instance of the exponential or linear models. The mode of the  $r_{\text{b}}$  distribution is shifted to  $1.49 \text{ kpc}$  ( $2.70 r_{\text{b},0}$ ) from  $1.28 \text{ kpc}$ . By construct, the sigmoid function is not as sensitive to large values of  $v_{\text{kick}}$  (compared to the exponential and linear models) if the function plateau is constrained to recoil velocities within our sampled range, as  $v_{\text{kick}} \rightarrow r_{\text{b}}$  and  $v_{\text{kick}} + \delta v_{\text{kick}} \rightarrow \sim r_{\text{b}}$ .

Despite the three models mapping SMBH recoil velocities  $0 \leq v_{\text{kick}} / \text{km s}^{-1} \leq 1020$  to  $r_{\text{b}}$  with a similar level of accuracy, as revealed by the  $\widehat{\text{ELPD}}$  measure, we argue that the sigmoid model is the overall preferred model when considering an unconstrained SMBH recoil velocity distribution. The response of the stellar system to SMBH recoil velocities greater than the escape velocity of the system should be consistent, irrespective of how much greater  $v_{\text{kick}}$  is than  $v_{\text{esc}}$ . This behaviour is not captured with the exponential nor linear models. For example, in the case of the sigmoid model, a scaled recoil velocity ( $v' = v/v_{\text{esc}}$ ) of  $v' = 2 \rightarrow r_{\text{b}} = 3.9$ , whereas  $v' = 4 \rightarrow r_{\text{b}} = 4.0$ . Conversely, for the exponential model,  $v' = 2 \rightarrow r_{\text{b}} = 5.7$ , whereas  $v' = 4 \rightarrow r_{\text{b}} = 9.0$ . From this argument, we suggest the sigmoid model to be the preferred model when considering the core radius produced by arbitrary SMBH recoil velocity.

Irrespective of using the full distribution of SMBH recoil velocities predicted by the Zlochower & Lousto (2015) model, or a truncated distribution thereof, a recoiling SMBH serves to enhance the stellar core formed by the SMBH binary prior to merger typically by a factor of 2–3. This leads to core sizes in excess of a kiloparsec, which is also seen in observations (e.g. Thomas et al. 2016; Dullo 2019).

## 5 ORBIT ANALYSIS

Having established from a forward-modelling point of view that a changing SMBH recoil velocity induces a systematic effect in the mass distribution of the galaxy remnant, we turn our attention to inferring the occurrence of an SMBH that has experienced a recoil velocity, based on the snapshot when the SMBH is seen to be settled. To this end, we perform an orbit analysis of the merger remnants in our sample following Frigo et al. (2021), which is briefly described here.

First, the merger remnant is rotated so that the  $z$ -axis coincides with the minor axis of the reduced inertia tensor (equation A1) as measured using the top 50 per cent most bound stellar particles to the stellar centre of mass. We then need to fit the gravitational potential of the system, which we do so by using a self-consistent field (SCF)

**Table 3.** Classification of orbital families.

Family	Description
Inner $x$ -tube	Rotate about the major axis of the galaxy, but move radially when far from centre (concave shaped)
Outer $x$ -tube	Rotate about the major axis of the galaxy (convex shaped)
$z$ -tube	Rotate about the minor axis of the galaxy
$\pi$ -box	Non-resonant motion with no net angular momentum (radial motion)
Boxlet	Resonant motion with no net angular momentum
Rosette	Typical orbit in a point-mass dominated spherically-symmetric potential
Irregular	No integrals of motion
Unclassified	Orbits unable to be classified

potential (Hernquist & Ostriker 1992; Jesseit, Naab & Burkert 2005; Röttgers et al. 2014), representing the potential  $\Phi(\mathbf{x})$  generated by the particles in the simulation as a combination of harmonics with expansion coefficients  $A$ :

$$\Phi(\mathbf{x}) = \sum_{nlm} A_{nlm} \Phi_{nlm}(\mathbf{x}), \quad (24)$$

where each individual harmonic independently satisfies the Poisson equation. The coefficients  $A_{nlm}$  describe the order  $n$  the radial component of the potential is expanded to, and to which order  $l$ ,  $m$  the angular components are expanded; the angular dependence is a (somewhat complicated) function of the spherical harmonics  $Y_{lm}(\theta, \phi)$ , where  $|m| < l$  as usual. The zeroth order of the potential expansion  $\Phi_{000}(\mathbf{x})$  is the model upon which we wish to construct our expansion, and a common choice for this is the Hernquist (1990) profile. Following Frigo et al. (2021), the expansion is limited to  $n_{\max} = 18$  and  $l_{\max} = 7$ , as this captures the potential of the galactic merger remnant with sufficient accuracy.

The chosen basis functions are unable to describe a point-mass potential, thus complicating the simulations for which the SMBH was settled at the centre. To overcome this, we centre the snapshot on the SMBH position, but exclude the SMBH from the SCF routine. This provides us with a potential field without the SMBH contribution; the potential from the SMBH is then added as a point-mass potential following the SCF potential construction. In the case where the SMBH has not settled at the centre (i.e. the  $v_{\text{kick}} = 2000 \text{ km s}^{-1}$  simulation) we simply align the snapshot with the centre of mass determined using the shrinking sphere method on stellar particles, and neglect the contribution from the SMBH (as it is very far from the centre and thus no longer influences the orbits of the stellar particles). We now have a representation of the potential in an analytical form in which the orbits of individual stellar particles can be integrated. The potential of the merger remnant is checked for stability by comparing the potential from the SCF method to the potential computed from the particle data by GADGET-4 during the simulation, and ensuring the ratio of the two is  $\sim 1$  at all radii.

Each stellar particle within  $2R_e \simeq 11 \text{ kpc}$  of the centre is integrated for fifty orbits to determine which, if any, orbital resonances exist.<sup>5</sup> The orbital resonances define the different families of orbits, as given in Frigo et al. (2021), and are listed in Table 3. We then determine the

<sup>5</sup>As each stellar particle is integrated in a fixed potential, the effect of two-body interactions are not captured by this method.

fraction of each orbital family in ten logarithmically spaced radial bins extending from 0.2 to 11 kpc.

Three distinct trends are made apparent in Fig. 9. The first is the increase in the fraction of  $\pi$ -box orbits with increasing recoil velocity, most notable at radii  $r \lesssim 5 \text{ kpc}$ . The simulation with  $v_{\text{kick}} = 2000 \text{ km s}^{-1}$  noticeably stands out, with the fraction of  $\pi$ -box orbits being  $\sim 0.6$  at the innermost radii. Complementary but converse to the first trend, increasing the SMBH recoil velocity marginally decreases the fraction of  $z$ -tube orbits from  $\sim 0.2$  to  $\lesssim 0.1$  within 1 kpc. Again the  $v_{\text{kick}} = 2000 \text{ km s}^{-1}$  is noticeably offset from the other simulations, however remains consistent with the general trend. Finally, increasing the SMBH recoil velocity decreases the fraction of rosette orbits at small radii  $r < 1 \text{ kpc}$ , with no rosette orbits for the  $v_{\text{kick}} = 2000 \text{ km s}^{-1}$  simulation. There is evidence for a minor decrease in outer  $x$ -tube orbits with increasing recoil velocity at radii  $r < 3 \text{ kpc}$ , however this trend is not as dramatic as the three previously discussed. In particular, the  $v_{\text{kick}} = 2000 \text{ km s}^{-1}$  simulation has almost no outer  $x$ -tube orbits until  $r = 2 \text{ kpc}$ , and only comes to dominate the orbit fraction at  $r \sim 10 \text{ kpc}$ .

We can naturally explain the decrease in rosette orbits with increasing recoil velocity by considering that a rosette orbit requires a point-mass like potential to orbit in. With a larger recoil velocity, we are displacing the SMBH increasingly further from the stellar centre of mass, thus disrupting the conditions required to maintain such an orbit. A consequence of disrupting these regular, rosette orbits, is the inducement of more radial orbits as recoil velocity grows, manifested as an increase in non-resonant  $\pi$ -box orbits. With a settled SMBH dominating the potential at the centre of the merger remnant, stellar orbits may slowly diffuse through relaxation processes to form rosette orbits at times  $t > t_{\text{settle}}$ . However, the time-scale required for boxlet and  $\pi$ -box orbits to acquire sufficient angular momentum to become rosette orbits is very long; as discussed in Section 3.4, relaxation processes do not dominate the centre of the galaxy over the time-scales relevant for these simulations, and violent relaxation is not applicable in the instance of a single SMBH.

We show the orbit families as a function of radius organized by recoil velocity in Fig. 10, instead of family class. At intermediate radii ( $r > 2 \text{ kpc}$ ), outer  $x$ -tube orbits dominate over all other families for all simulations, a distinct feature of prolate systems. The merger remnants in this study are predominantly prolate rotators at the time of analysis (see bottom panel of Fig. A1), in agreement with results from previous simulation studies of major mergers (e.g. Naab & Burkert 2003; González-García et al. 2009; Ebrova & Lokas 2017). Interestingly, increasing the recoil velocity pushes the intersection of boxlet and  $z$ -tube orbits to increasingly larger radii, from  $\sim 1.5 \text{ kpc}$  for  $v_{\text{kick}} = 0 \text{ km s}^{-1}$  to  $\sim 3 \text{ kpc}$  for  $v_{\text{kick}} = 1020 \text{ km s}^{-1}$ . Finally, for the  $v_{\text{kick}} = 2000 \text{ km s}^{-1}$  simulation, the dominance of  $\pi$ -box orbits over all other families is apparent for radii  $r \lesssim 8 \text{ kpc}$ . This is the only recoil velocity for which  $\pi$ -box orbits are the dominant orbital family; in the simulations with  $v_{\text{kick}} \leq 1020 \text{ km s}^{-1}$ ,  $\pi$ -box orbits are always subdominant to boxlet orbits.

Further insight is provided by grouping the orbital families into two broad classes, ‘boxes’ and ‘tubes’. Those orbits which do not have a net angular momentum we collectively refer to as boxes, and include boxlet and  $\pi$ -box orbits. Similarly, those orbits which do have some net angular momentum we collectively refer to as tubes, and include the two types of  $x$ -tubes,  $z$ -tubes, and rosette orbits. The amount of stellar mass within the median core radius  $r_b$  for these two broad classes is shown in Fig. 11, where the points are coloured by the SMBH recoil velocity.

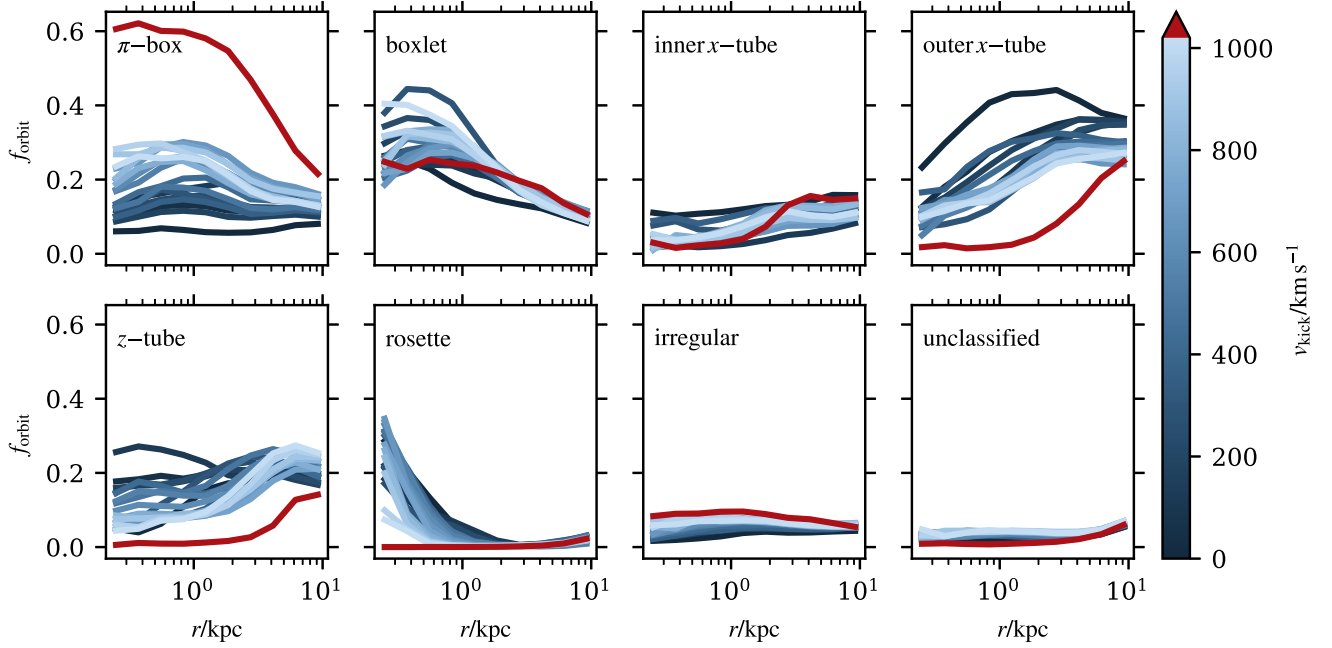


**Figure 9.** Orbit analysis of the merger remnants, with a consistent colour scheme to Fig. 3. Stellar particles are assigned to one of eight different orbital families, and binned into ten logarithmically spaced radial shells such that  $0.2 \leq R/\text{kpc} \leq 11.0$ . Noticeably, increasing recoil velocity induces a higher fraction of  $\pi$ -box orbits at all radii, and a complementary decrease in rosette orbits at radii  $r \lesssim 1$  kpc.

Immediately we see that for low kick velocities,  $v_{\text{kick}} \leq 180 \text{ km s}^{-1}$ , tube orbits dominate the merger remnant core. In particular, the  $v_{\text{kick}} = 0 \text{ km s}^{-1}$  case has the greatest ratio of tube to box orbits within the core,  $M_{\star, \text{tube}}/M_{\star, \text{box}} = 2.0$ . This is in agreement with an SMBH binary preferentially ejecting box orbits which lie within the loss cone during the three-body scattering phase.

Increasing the SMBH recoil velocity, there is a strong tendency for box orbits to dominate the core region, in some cases contributing more than  $6.0 \times 10^8 M_{\odot}$  of stellar mass ( $\sim 0.1 M_{\star}$ ), compared to some  $3.5 \times 10^8 M_{\odot}$  provided by tube orbits. The recoil velocity where the transition from a tube orbit-dominated core to a box orbit-dominated core occurs is around  $v_{\text{kick}} \sim 240 \text{ km s}^{-1}$ , approximately the same recoil velocity that allows the kicked SMBH to exit the SMBH binary-scoured core (see Fig. 2, upper panel). This suggests that as the kicked SMBH ploughs through the stellar core whilst it is settling but before its velocity falls below the velocity dispersion of the core, the rapid change in potential disrupts the conditions for angular momentum-conserving orbits, altering the stellar particles to radial orbits instead. For the highest kick velocities,  $v_{\text{kick}} > 900 \text{ km s}^{-1}$ , the amount of stellar mass in box orbits is almost twice that in tube orbits, as shown in Fig. 11.

In summary, a recoiling SMBH exiting the core leaves an imprint in the stellar orbits as it settles. Consequently, the stellar kinematics are also affected by the SMBH motion.

## 6 STELLAR KINEMATICS

### 6.1 Integral field unit kinematics

We next create mock integral field unit (IFU) observations using two different projections for the line-of-sight (LOS) velocity distribution: one where the LOS is along the SMBH kick axis (‘parallel’), and another where the LOS is along an axis orthogonal to the SMBH

kick axis (‘orthogonal’). Testing these two special projections, we investigate the limiting cases of how the galaxy kinematics behave when all or none of the SMBH motion is directed along the LOS to the observer.

We create our mock IFU observations following Naab et al. (2014), assuming our merger remnants represent local elliptical galaxies that lie at  $z = 0.01$ . Our observations encompass a square aperture of side length  $0.25 r_{1/2}$ , where  $r_{1/2}$  is the 3D half-mass radius. For each particle within this aperture, we generate 25 pseudo-particles with identical LOS velocities as the original particle, but are spatially displaced from the original particle with a Gaussian distribution in the projected  $x$  and  $y$  direction with a standard deviation of  $6.8 \text{ arcsec}$  (corresponding to a physical scale<sup>6</sup> of  $0.3 \text{ kpc}$  at  $z = 0.01$ ) to mimic seeing effects. The pseudo-particles are then binned onto a spatial grid, where the grid is assumed to have a resolution of  $0.2 \text{ arcsec}$ , similar to the observations of Neureiter et al. (2023), which then corresponds to a physical resolution of  $\sim 0.04 \text{ kpc}$ . Following the method in Cappellari & Copin (2003), we then group adjacent bins into larger Voronoi bins to achieve a particle number of  $\sim 50$  000 particles per Voronoi bin.

For each Voronoi bin, we follow van der Marel & Franx (1993) and decompose the LOS velocity into a series of Gauss–Hermite functions, described by the mean radial velocity  $V$ , the velocity dispersion  $\sigma$ , asymmetric deviation  $h_3$ , and symmetric deviation  $h_4$ . The line profile is thus described by:

$$\mathcal{L} = \frac{1}{\sqrt{2\pi}\sigma} e^{-w^2/2} \left\{ 1 + \sum_{j=3}^4 h_j H_j(w) \right\}, \quad (25)$$

<sup>6</sup><https://cosmocalc.icrar.org> with  $\Lambda$ CDM cosmological parameters  $H_0 = 70 \text{ km s}^{-1} \text{ Mpc}^{-1}$ ,  $\Omega_M = 0.3$ , and  $\Omega_{\Lambda} = 0.7$ .

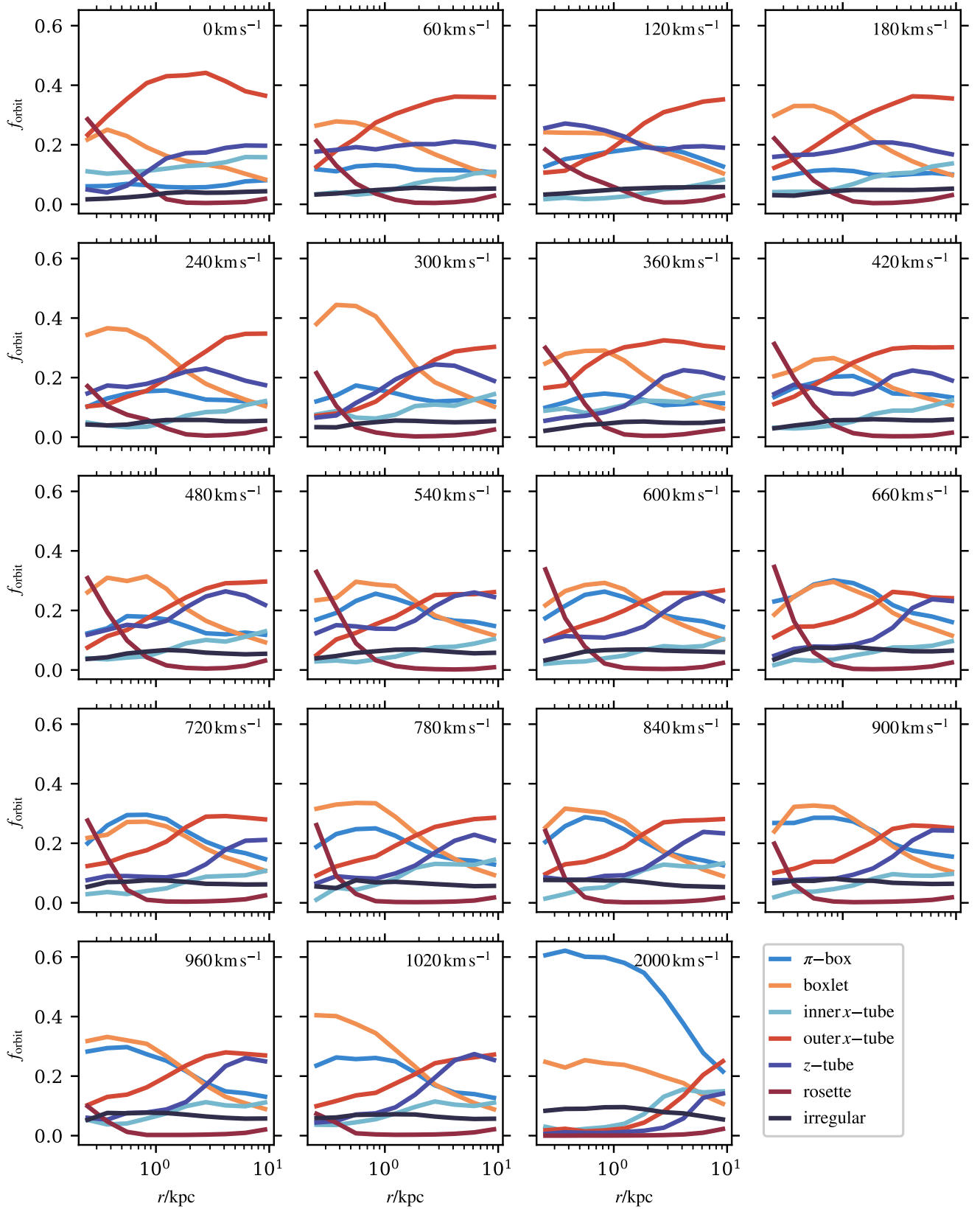


**Figure 10.** Same as Fig. 9, but each merger remnant is shown in its own panel, with the different orbital families depicted by colour, to better demonstrate the radial fraction of orbits for a given merger. Note that the orbits that were unable to be classified are not shown in this plot.

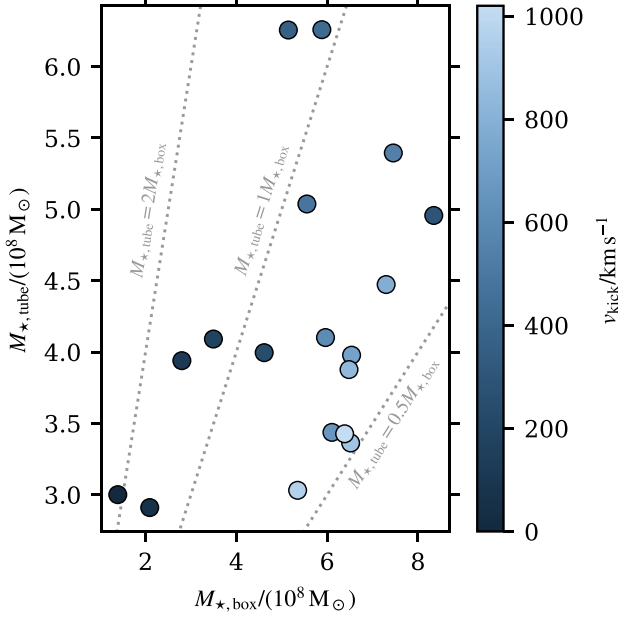


**Figure 11.** Amount of stellar mass classified as box orbits (boxlet or  $\pi$ -box) compared to tube orbits ( $x$ -tubes,  $z$ -tube, or rosette) within the median core radius  $r_b$  for each simulation. Points are coloured by kick velocity. Simulations with low  $v_{\text{kick}}$  predominantly contain tube orbits within  $r_b$ , whereas larger recoil velocities have a tendency for box orbits to dominate.

where  $w \equiv (v_{\text{LOS}} - V)/\sigma$ , and the Hermite polynomials  $H_3$  and  $H_4$  are defined:

$$\begin{aligned} H_3 &= \frac{1}{\sqrt{3}}(2w^3 - 3w) \\ H_4 &= \frac{1}{\sqrt{24}}(4w^4 - 12w^2 + 3). \end{aligned} \quad (26)$$

Relative to a standard Gaussian (which has  $h_4 = 0$ ), a positive value of  $h_4$  corresponds to extended high velocity tails in the LOS velocity distribution and a more peaked distribution about the mean value  $V$ . Conversely, a negative value of  $h_4$  corresponds to weaker tails in the LOS velocity distribution and a broader distribution of LOS velocities about the mean value  $V$ . A recent comprehensive study of LOS velocity distribution fitting applied to elliptical galaxies can be found in Mehrgan et al. (2023).

We show example IFU maps for the parallel projections of the  $v_{\text{kick}} = 0 \text{ km s}^{-1}$  case in Fig. 12, and of the  $v_{\text{kick}} = 600 \text{ km s}^{-1}$  case in Fig. 13. In both figures, the first row corresponds to mock observations of all stellar particles within the square aperture, the second row corresponds to the subset of particles classified as box orbits, and the third row corresponds to the subset of particles classified as tube orbits. The first column of each figure depicts the ordered rotation  $V$  of the stellar particles, the second column shows the velocity dispersion  $\sigma$ , the third column shows the coefficient of asymmetric deviation  $h_3$ , and the fourth column shows the coefficient of symmetric deviation  $h_4$ . The core radius of the merger remnant, as determined in Section 4.2, is depicted with a dashed ring in each panel.

We first note that all our simulated merger remnants have almost negligible rotation, as immediately seen in the ordered rotation maps of Figs 12 and 13. Quantitatively, the dimensionless spin parameter is a useful measure to assess the level of rotation (Emsellem et al.

2007), and is defined:

$$\lambda_R = \frac{\sum_{i=1}^N F_i R_i |V_i|}{\sum_{i=1}^N F_i R_i \sqrt{V_i^2 + \sigma_i^2}}, \quad (27)$$

where  $F_i$  is the flux,  $R_i$  is the radial displacement from the centre,  $V_i$  is the mean velocity, and  $\sigma_i$  is the velocity dispersion, each taken within the  $i$ -th Voronoi bin. We find that our galaxies have  $\lambda_R < 0.02$  within the IFU aperture, and thus we conclude that very little rotation is present.

For the  $v_{\text{kick}} = 0 \text{ km s}^{-1}$  case in Fig. 12, we first note an interesting structure in the ordered rotation  $V$  of all stellar particles. There is a hint of rotation occurring about the  $z = 0$  axis, however a counter-rotating structure is present close to the  $y = 0$  axis (keeping in mind that as previously discussed, overall the magnitude of this rotation is very minimal). This feature is also seen in the mock IFU images of the tube orbits. Additionally, creating mock IFU maps for two other projections (one with the line-of-sight aligned with the major axis of the inertia tensor, and the other with the line-of-sight aligned with the vector normal to the merger plane), this feature is not present. We thus conclude that immediately following the merger of an SMBH binary, complex structure in the LOSVD may be apparent for tube orbits.

The kinematic features for the second, third, and fourth moments of the LOSVD are not as sensitive to the viewing angle, with box orbits displaying a centrally peaked velocity dispersion compared to a spatially homogeneous velocity dispersion for tube orbits. The spatial extent of the centrally peaked velocity dispersion extends beyond the core radius when viewing all stellar particles, however is overall reduced in magnitude compared to the box orbits owing to the inclusion of the tube orbits. A peaked central velocity dispersion can be naturally explained for box orbits owing to the radial motion of these particles increasing in velocity closer to the centre of the potential, when these particles are at their pericentre.

Another curious feature is an annulus of negative  $h_4$  that is clearly visible for box orbits, but is absent in the  $h_4$  maps for tube orbits and all stellar particles. At the centre of the annulus,  $h_4 \sim 0$ , with the inner ring of the annulus coinciding with the core radius. The region of negative  $h_4$  in the IFU maps of the box orbits can be understood as the population of box orbits which did not interact with the SMBH binary prior to coalescence. The positive  $h_4$  beyond the annulus is a result of the box orbits reaching apocentre, where the velocity becomes zero (irrespective of orientation), thus resulting in an overly peaked LOSVD. From Fig. 11, for  $v_{\text{kick}} = 0 \text{ km s}^{-1}$  there is more stellar mass in tube orbits than box orbits within the core (and at radii  $r > r_b$ , shown by the increased number of Voronoi cells for tube orbits in Fig. 12 compared to box orbits). More tube orbits leads to the  $h_4$  annulus being absent in the map of  $h_4$  for all stellar particles.

Turning our attention to the IFU maps in Fig. 13 for the  $v_{\text{kick}} = 600 \text{ km s}^{-1}$  case, we notice immediately that ordered rotation about the  $z = 0$  axis is minimal, and the velocity dispersion for all stellar particles has a centrally peaked structure that extends to the core radius. Converse to the  $v_{\text{kick}} = 0 \text{ km s}^{-1}$  case the core radius extends to the same radius as the enhanced velocity dispersion in the box orbits.

Similar to the  $v_{\text{kick}} = 0 \text{ km s}^{-1}$  case, an annulus of negative  $h_4$  is present for the  $v_{\text{kick}} = 600 \text{ km s}^{-1}$  simulation. However, the core radius has expanded beyond the central  $h_4 \sim 0$  region to encompass some of the annulus. Owing to the box orbit-dominated core (from Fig. 11,  $M_{*,\text{tube}}/M_{*,\text{box}} \sim 0.75$ ), the annulus of negative  $h_4$  is now present in the  $h_4$  kinematic map for all stellar particles. Critically



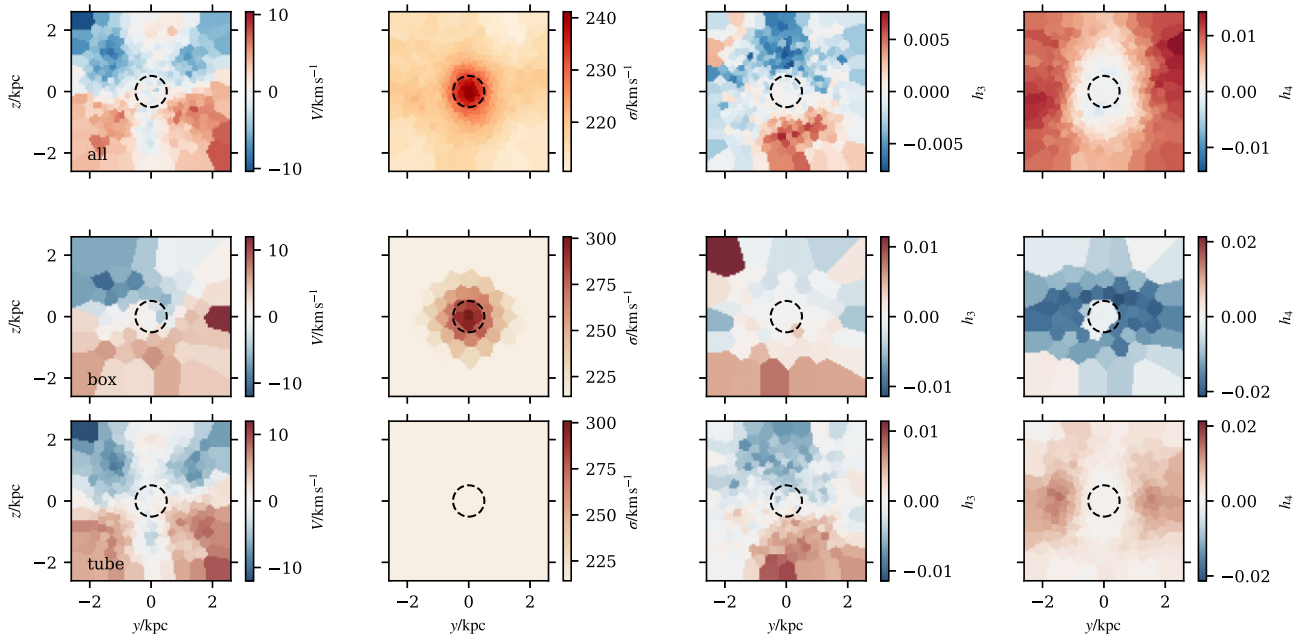


**Figure 12.** Mock integral field unit kinematic maps of the  $v_{\text{kick}} = 0 \text{ km s}^{-1}$  remnant stellar particles in the parallel projection at the time the SMBH has settled. The IFU maps extend out to  $0.25 r_{1/2}$  in a square aperture. The top row shows the IFU maps for each of the ordered rotation  $V$ , velocity dispersion  $\sigma$ , asymmetric deviation coefficient  $h_3$ , and symmetric deviation coefficient  $h_4$ , for all stellar particles within the square aperture. The second row shows the IFU maps for those stellar particles within the aperture classified as box orbits, and the third row shows the complementary IFU maps for those stellar particles within the aperture classified as tube orbits. The dashed circle indicates the core radius  $r_b$  of the merger remnant. For the box and tube orbit rows, the colour scale is consistent for each column, however the colour scale is different for the top row. The ordered rotation  $V$  is generally correlated with  $h_3$ . A centrally peaked velocity dispersion is only visible in box orbits and not tube orbits, as is an annulus of negative  $h_4$ . Almost no negative  $h_4$  is present in the IFU map for all stellar particles. From Fig. 11, this simulation has  $1.4 \times 10^8 M_{\odot}$  stellar mass in box orbits, and  $3.0 \times 10^8 M_{\odot}$  stellar mass in tube orbits, within  $r_b$ .

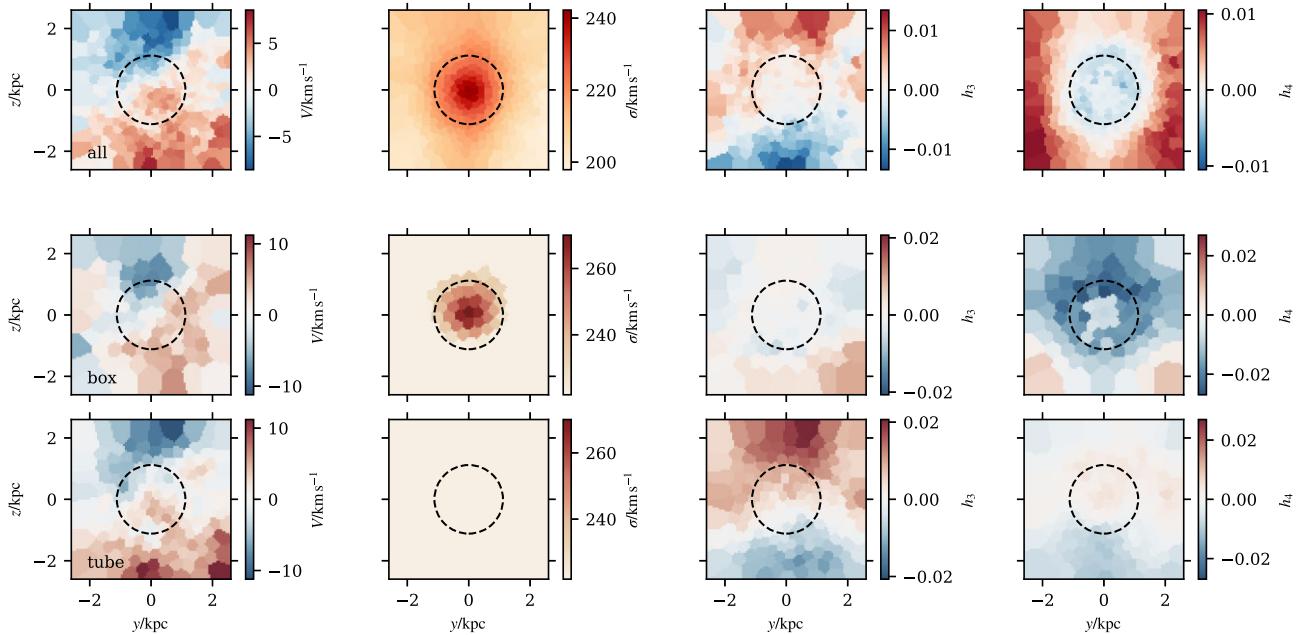


**Figure 13.** Similar to Fig. 12, mock integral field unit kinematic maps of the  $v_{\text{kick}} = 600 \text{ km s}^{-1}$  remnant stellar particles in the parallel projection at the time the SMBH has settled. From Fig. 11, this simulation has  $5.9 \times 10^8 M_{\odot}$  stellar mass in box orbits, and  $4.1 \times 10^8 M_{\odot}$  stellar mass in tube orbits, within  $r_b$ . Similar to the  $v_{\text{kick}} = 0 \text{ km s}^{-1}$  case, a peaked velocity dispersion is visible for all stellar particles, but this contribution comes solely from the box orbits. An annulus of negative  $h_4$  is seen to extend to the core radius in the IFU map for all stellar particles, and for box orbits.

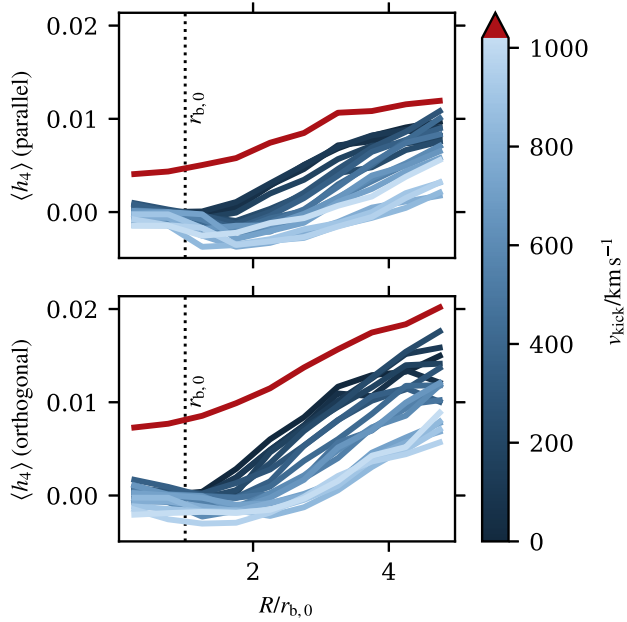


**Figure 14.** Annuli-averaged  $h_4$  parameter for the parallel (top panel) and orthogonal (bottom panel) projections. For both the parallel and orthogonal projections, for those simulations with  $v_{\text{kick}} \leq 1020 \text{ km s}^{-1}$  (i.e. have their SMBHs settled), there is a systematic decrease in the  $h_4$  parameter with increasing  $v_{\text{kick}}$  for  $v_{\text{kick}} \lesssim 720 \text{ km s}^{-1}$ . For  $720 \lesssim v_{\text{kick}}/\text{km s}^{-1} \leq 1020$ , the  $h_4$  parameter is indistinguishable from each other. For the  $v_{\text{kick}} = 2000 \text{ km s}^{-1}$  case, the  $h_4$  is both positive and significantly larger than the  $720 \lesssim v_{\text{kick}}/\text{km s}^{-1} \leq 1020$  simulations, for both parallel and orthogonal projections.

however, a central region of  $h_4 \sim 0$  is present in the map for all stellar particles, and corresponds to the same spatial extent of the  $h_4 \sim 0$  region in the  $v_{\text{kick}} = 0 \text{ km s}^{-1}$  simulation. We propose that this central region of  $h_4 \sim 0$  is indicative of the core radius due solely to SMBH binary scouring  $r_{\text{b},0}$ , prior to any core enhancement by the recoiling SMBH, and set about identifying the radial extent of this region.

## 6.2 Radial trends in $h_4$

To quantify the radial dependence of  $h_4$ , we bin the Voronoi cells into ten concentric annuli out to  $5r_{\text{b},0}$ , and take the median  $h_4$  value within each annulus, denoting this as  $\langle h_4 \rangle$ .

The radial dependence of  $\langle h_4 \rangle$  is shown in Fig. 14. Aside from the  $v_{\text{kick}} = 2000 \text{ km s}^{-1}$  simulation, increasing the kick velocity results in progressively more negative  $\langle h_4 \rangle$  in both the parallel and orthogonal projections at radii  $R \gtrsim 1 \text{ kpc}$ , seen as an overall downward shift in Fig. 14. The value of  $\langle h_4 \rangle$  saturates for simulations with  $v_{\text{kick}} \gtrsim 720 \text{ km s}^{-1}$ , with a minimum of  $\langle h_4 \rangle < 0$  at  $R \sim 1 \text{ kpc}$  for both the parallel and orthogonal projections.

As discussed in Section 6.1, identifying the radius at which  $\langle h_4 \rangle$  starts to become negative can give insight to the core size due solely to SMBH binary scouring. For the parallel projection,  $\langle h_4 \rangle$  starts to become negative at  $R \sim 0.5 \text{ kpc}$ , and  $R \sim 0.6 \text{ kpc}$  for the orthogonal projection, irrespective of the recoil velocity  $v_{\text{kick}}$ . Both of these values are in good agreement with the known core size due to binary scouring of  $0.58 \text{ kpc}$  discussed in Section 3.2, as indicated by the vertical dotted line in Fig. 14.

To understand the overall trends in Fig. 14, we must refer to the orbit analysis of Section 5. Within  $R \sim 1 \text{ kpc}$ , the  $\langle h_4 \rangle$  profiles are largely consistent between kick velocities. The dominant orbital family within this radius for simulations with recoil velocities  $60 \leq v_{\text{kick}}/\text{km s}^{-1} \leq 1020$  is the boxlet family: radial orbits which can reach arbitrarily close to the centre. As these orbits approach their pericentre at small radii, the different projections of these boxlet orbits result in a LOSVD that is relatively broad around the mean, resulting in a value of  $\langle h_4 \rangle$  that is either 0 or slightly negative, irrespective of the SMBH recoil velocity. This also explains the consistency in  $\langle h_4 \rangle$  between the parallel and orthogonal projections at small radii.

At radii beyond  $R \sim 1 \text{ kpc}$ , there is a strong tendency, at a given radius, for simulations with a low  $v_{\text{kick}}$  to have a higher value of  $\langle h_4 \rangle$  than simulations with a high  $v_{\text{kick}}$ . From Fig. 10, this is also the radius at which the dominant orbital family transitions from boxlet orbits to  $x$ -tube orbits for simulations with  $60 \leq v_{\text{kick}}/\text{km s}^{-1} \leq 1020$ , though boxlet orbits are by no means negligible. Additionally, when considering the apocentre distribution of stellar particles with a mean position within  $\sim 0.25r_{1/2}$  (Fig. C1), the distributions are all left-skewed, and become increasingly left-skewed with increasing  $v_{\text{kick}}$ . At apocentre, a stellar particle on a radial orbit will have a zero velocity vector, which is then viewed as a zero velocity vector when projected to an observer. Similarly, for stellar particles on non-radial orbits, the apocentre represents a minimum, but not necessarily zero, velocity.<sup>7</sup> In either case, the LOSVD peaks towards the mean velocity at apocentre, thus inducing a mildly positive  $\langle h_4 \rangle$ . As the peak of the apocentre distribution shifts to larger radii with increasing  $v_{\text{kick}}$ , we expect to find more stellar particles at apocentre at small radii for low  $v_{\text{kick}}$  simulations, than for high  $v_{\text{kick}}$  simulations. This in turn leads to an elevated value of  $\langle h_4 \rangle$  at small radii for simulations with low  $v_{\text{kick}}$  compared to those with high  $v_{\text{kick}}$ .

For the  $v_{\text{kick}} = 2000 \text{ km s}^{-1}$  simulation, where the SMBH did not return to the centre of the merger remnant, the radial  $\langle h_4 \rangle$  profile is clearly different to those simulations in which the SMBH managed to return to the centre. Here, the  $\langle h_4 \rangle$  profile is elevated compared to the lower  $v_{\text{kick}}$  simulations at all radii in both the parallel and orthogonal projections. Again, we can readily understand this phenomenon with the orbital analysis in Section 5. In Fig. 10, we clearly see that  $\pi$ -box and boxlet orbits dominate over all other orbital families in the radial range covered by the mock IFU maps. Additionally, the apocentre distribution of the  $v_{\text{kick}} = 2000 \text{ km s}^{-1}$  simulation peaks at smaller radii than the majority of the simulations with a settled SMBH: it is less left-skewed, indicating that more particles have their apocentre at radii covered by the mock IFU maps. By the same reasoning as above, a higher concentration of apocentres at small radii narrows the LOSVD profile, resulting in an elevated value of  $\langle h_4 \rangle$ , and is seen in Fig. 14.

In the analysis of the kinematic maps, a complication arises from choosing the snapshot once the SMBH has settled, which as discussed in Section 3.2 varies as a function of recoil velocity. To explore the effect of our choice of snapshot, we redo the IFU analysis for various times following when the SMBH kick occurs. A representative example is shown in Fig. C2 for the case of  $v_{\text{kick}} = 900 \text{ km s}^{-1}$ . We take snapshots corresponding to times between 0.18 and 1.70 Gyr, in addition to the fiducial snapshot at 1.28 Gyr. Prior to the SMBH settling, the value of  $\langle h_4 \rangle$  fluctuates as the settling SMBH influences the surrounding stellar kinematics. The  $\langle h_4 \rangle$  profile is consistent for

<sup>7</sup>Except in the case where the motion is completely tangential to the observer, in which case there is no projected component of the velocity vector.

all times following the SMBH settling, and thus gives us confidence that, provided the SMBH has settled, the  $\langle h_4 \rangle$  profile is insensitive to the precise time of measurement. As a result, the differences in  $\langle h_4 \rangle$  profile presented in Fig. 14 are a result of the stellar mass distribution responding to the change in potential caused by the oscillating SMBH, and not due to general relaxation processes (refer also to Section 3.4).

### 6.3 Velocity anisotropy

As described in Section 5, SMBHs can induce a significant change in the radial distribution of the stellar orbital families. On a more global scale, the change in orbit distribution manifests as a stellar velocity anisotropy. A widely used measure for the velocity anisotropy of a given stellar system is the anisotropy parameter  $\beta$  (Binney & Tremaine 2008) given by

$$\beta = 1 - \frac{\sigma_\theta^2 + \sigma_\phi^2}{2\sigma_r^2}, \quad (28)$$

where  $\sigma_\theta$ ,  $\sigma_\phi$ , and  $\sigma_r$  are the components of the stellar velocity dispersion in spherical coordinates. Stellar systems with  $\beta < 0$  are referred to as ‘tangentially biased’ systems, whereas  $\beta > 0$  corresponds to ‘radially biased’ systems. A stellar system with purely radial orbits ( $\sigma_\theta = \sigma_\phi = 0$ ) corresponds to  $\beta = 1$ , while purely circular orbits ( $\sigma_r = 0$ ) would yield  $\beta = -\infty$ . An ergodic system is one where  $\sigma_\theta = \sigma_\phi = \sigma_r \iff \beta = 0$ , and hence corresponds to a balance between box and tube orbits.

Prior to their eventual merger, SMBH binaries can interact strongly with the stellar particles in their vicinity via three-body scattering. However, in order to undergo a strong interaction, the stellar particle must come sufficiently close to the SMBH binary. Such stellar particles are predominantly on radial orbits with small pericentre distances and low angular momenta, which enables them to reach the centre of the galaxy: they belong to the loss cone of the SMBH binary. As a consequence, SMBH binaries are expected to induce tangentially biased cores in the central regions of their host galaxies by primarily ejecting stellar particles on radial orbits (e.g. Quinlan & Hernquist 1997; Milosavljević & Merritt 2001; Thomas et al. 2014; Rantala et al. 2018, 2019). Recoiling SMBHs, on the other hand, can induce velocity anisotropy by changing the shape of the local gravitational potential as described in Section 5. Rosette orbits, for instance, are easily disturbed by a recoiling SMBH: as the potential in the initial position of the SMBH becomes non-spherical, stars initially on rosette orbits can move onto  $\pi$ -box orbits, which manifests as additional tangential bias in the central regions of the galaxy.

Fig. 15 shows the anisotropy parameter  $\beta$  as a function of  $v_{\text{kick}}$  for the merger simulations once the SMBH has settled, for  $v_{\text{kick}}$  between 0 and 1020  $\text{km s}^{-1}$ . For each simulation, the stellar particles are divided into two radial bins corresponding to  $r \leq r_b$  (blue points) and  $r > r_b$  (orange points), where the core radius  $r_b$  is Monte Carlo sampled  $N = 10^4$  times for each simulation from its marginal  $r_b$  posterior distribution (Section 4.2). The final  $\beta$  and the corresponding error are obtained as the median and interquartile range across the entire sample for each merger remnant.

As is evident from Fig. 15, the merger remnants with  $v_{\text{kick}} \leq 180 \text{ km s}^{-1}$  have tangentially biased ( $\beta < 0$ ) stellar populations within  $r_b$ . This is consistent with Fig. 11, in which increasing the kick velocity is shown to induce a lower fraction of angular momentum-conserving orbits ( $x$ -tube,  $z$ -tube, and rosette) and a higher fraction of radial orbits ( $\pi$ -box and boxlet) in the inner regions. For larger kick velocities ( $v_{\text{kick}} \gtrsim \sigma_{*,0}$ ), the  $\beta$  parameter for stellar particles

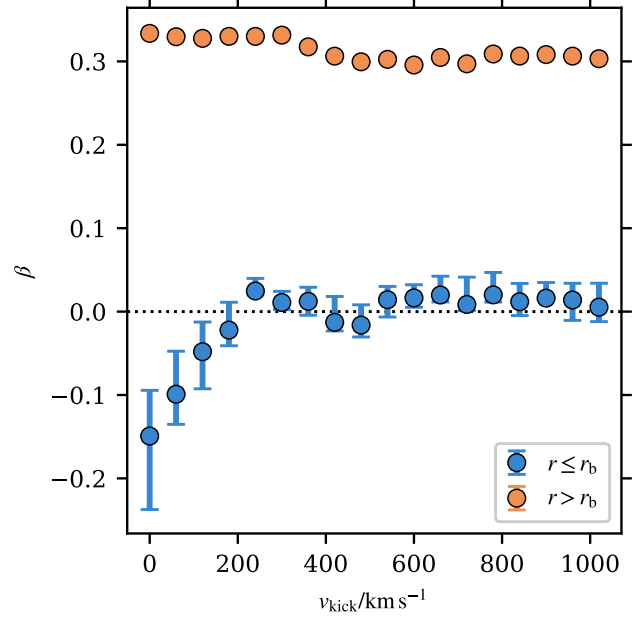


**Figure 15.** Stellar velocity anisotropy parameter  $\beta$  as a function of the kick velocity  $v_{\text{kick}}$ . The stellar particles are divided into two radial bins with  $r \leq r_b$  and  $r > r_b$ , where the core radius  $r_b$  is sampled  $N = 10^4$  times for each simulation from its marginal  $r_b$  posterior distribution. The final value for  $\beta$  and the corresponding error are computed as the median and interquartile range across the entire sample (note for the orange points, the error is smaller than the marker). The blue and orange points correspond to the inner and outer bins, respectively, while the dotted horizontal line indicates an ergodic system with  $\beta = 0$ . Only simulations with  $v_{\text{kick}} \leq 180 \text{ km s}^{-1}$  display tangential bias ( $\beta < 0$ ) for  $r \leq r_b$ , whereas all simulations are radially biased for  $r > r_b$ .

within  $r_b$  is consistent with an ergodic system. This results from the growth of the core radius with increasing  $v_{\text{kick}}$  shown in Fig. 7: as  $r_b$  increases, the enlarged core region encompasses stellar particles on box orbits which were not ejected by the SMBH binary prior to coalescence, as demonstrated by the IFU maps in Fig. 13. These stellar particles, found at radii  $r_{b,0} < r < r_b$  (recalling that  $r_{b,0}$  is the core radius due to SMBH binary scouring only), have apocentres that in general increase with increasing kick velocity. As the said stellar particles pass radially within the core region, they increase the range of radial velocities within  $r_b$ , leading to a larger radial velocity dispersion so that  $2\sigma_r^2 \simeq \sigma_\theta^2 + \sigma_\phi^2$  and  $\beta \approx 0$  for the ergodic systems seen in Fig. 15. In this way, the anisotropy parameter  $\beta$  of the core region of an elliptical galaxy might give insight into whether or not the recoiling SMBH was ejected with a  $v_{\text{kick}}$  that removed it from the SMBH binary-scoured core.

For  $r > r_b$ , all merger remnants display a strong radial bias of  $\beta \gtrsim 0.3$ . This might initially seem contradictory with Fig. 9, which shows that the tangentially biased outer  $x$ -tube and  $z$ -tube orbits are the dominant orbital families at  $r \sim 10 \text{ kpc}$ . However, the stellar mass density decreases rapidly towards  $r \sim 10 \text{ kpc}$  as shown in Fig. 4 and hence the outer regions contribute only weakly to the overall  $\beta$  for  $r > r_b$ . Furthermore, the tangential bias of the aforementioned orbital families is weak at large radii, as shown in fig. 9 of Frigo et al. (2021), whereas the non-negligible  $\pi$ -box and boxlet orbits display strong radial bias at large radii. Finally, it is worth noting that the radial bias towards large radii is not induced by the recoiling SMBH: as is evident, the outer  $\beta$  bins of all merger remnants with  $v_{\text{kick}} > 0 \text{ km s}^{-1}$  are consistent with the  $v_{\text{kick}} = 0 \text{ km s}^{-1}$  remnant, which likewise

displays a strong radial bias for  $r > r_b$ . Instead, the radial bias is primarily induced by the (radial) merger orbit, which enables stellar particles to be deposited on radially biased orbits during the merger. A radially biased outer region is also predicted by cosmological galaxy formation models, in which the late-stage growth of elliptical galaxies is attributed to numerous minor mergers (e.g. Naab et al. 2009). As discussed in Rantala et al. (2018), further mergers would likely induce even stronger radial bias towards the outer regions and, assuming the inclusion of new SMBHs, also stronger tangential bias in the central regions.

## 7 DISCUSSION

### 7.1 Comparison to literature

In agreement with previous work (Boylan-Kolchin et al. 2004; Merritt et al. 2004), we find that an SMBH displaced due to gravitational recoil decreases the stellar density in the central regions of the merger remnant as it settles to an equilibrium state. Additionally, we find that this oscillatory motion, by the time the SMBH has settled, increases the size of the stellar density core beyond that induced by the scouring of the SMBH binary prior to coalescence, confirming the results of Gualandris & Merritt (2008), Nasim et al. (2021), and Khonji et al. (2024). We assess the magnitude of this scouring with time using the Lagrangian radii presented in Fig. 3. We see a sharp increase in the Lagrangian radii immediately after the SMBH binary coalesces. If the SMBH is kicked beyond the core, the SMBH generally does not pass through the core during the next few orbits due to tangential motion induced by the stellar potential torquing the SMBH. When the SMBH does pass through the core region in the last orbits when the SMBH velocity  $v_*$  is only marginally greater than the stellar velocity dispersion within the core, the Lagrangian radius rapidly increases further. Gualandris & Merritt (2008) found that each oscillation of the SMBH enlarges the core, whereas Nasim et al. (2021) found that only the initial oscillation due to the recoil kick affects the core. Our result suggest that differences in the torquing due to the specific distribution of stellar mass could alleviate some of the tension between the two studies.

The 3D stellar density profile (Fig. 4) appears centrally flat only in the instance where the SMBH escaped the galaxy entirely ( $v_{\text{kick}} = 2000 \text{ km s}^{-1}$ ). Conversely, a mild density cusp  $\rho \propto r^{-\nu}$  with  $0 < \nu < 1$  is present in simulations where the SMBH settled,  $v_{\text{kick}} < 1020 \text{ km s}^{-1}$ , with the exponent  $\nu$  decreasing with increasing  $v_{\text{kick}}$ , in agreement with previous work (e.g. Nasim et al. 2021; Khonji et al. 2024). All simulations with  $v_{\text{kick}} < 1020 \text{ km s}^{-1}$  display a core in projection however, in agreement with previous observational and theoretical work (e.g. Ferrarese et al. 1994; Nakano & Makino 1999).

The presence of a core in the 3D stellar density profile for  $v_{\text{kick}} = 2000 \text{ km s}^{-1}$  can be understood due to the lack of an SMBH at the centre of the remnant. The SMBH, which would ordinarily contribute a point-mass potential that acts as an attractor to stellar particles, is not present, and thus angular momentum-conserving rosette orbits are unable to form or be sustained, thus lowering the central stellar density. Instead, we observe  $\pi$ -box orbits to dominate at all radii for the  $v_{\text{kick}} = 2000 \text{ km s}^{-1}$  simulation, in tension with the understanding of box orbits being the dominant orbit family to interact with the SMBH binary prior to coalescence. However, we find that the excess of  $\pi$ -box orbits in the  $v_{\text{kick}} = 2000 \text{ km s}^{-1}$  simulation primarily originate from angular momentum-conserving orbits (63 per cent) which have reacted to a sudden change in the potential due to the escaping SMBH.

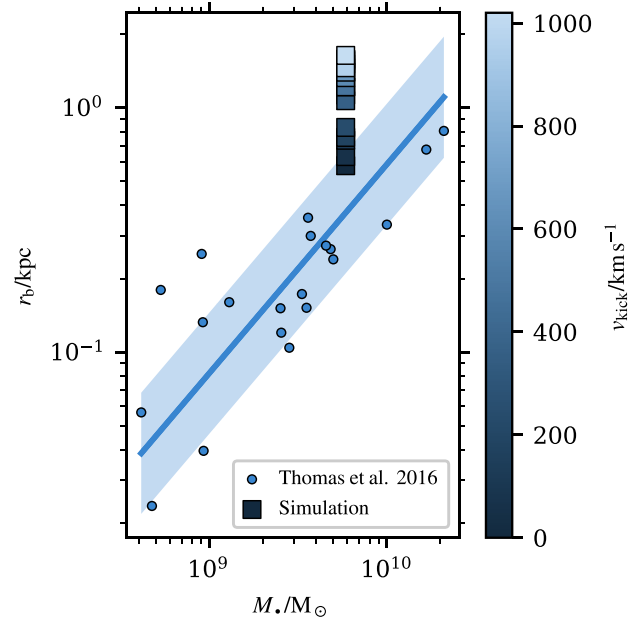


**Figure 16.** Comparison of the median measured core radii for each merger remnant to the observational data and the best-fitting constant-exponent power law presented in Thomas et al. (2016). The shaded region shows the reported intrinsic scatter of the relation. Only the merger remnants with very low  $v_{\text{kick}}$  lie within the intrinsic scatter of the relation, whereas remnants with large  $v_{\text{kick}}$  are significantly offset from the relation.

We caution that the claims made in Nasim et al. (2021), that cores produced by gravitational recoil of the coalesced SMBH are present in the 3D stellar density profile, has the caveat that the recoil velocity must remove the SMBH entirely from the centre of the galaxy remnant, where no oscillations passing through the core are possible. We find instead that arbitrary recoil kicks, which have a distribution generally peaking well below the escape velocity of the centre of the merger remnant, do not necessarily result in a truly flat 3D stellar density profile, however do produce a flatter density profile compared to the density profile produced by SMBH binary scouring alone.

### 7.2 Determining SMBH recoil velocity in observations

In Section 4.4, we determined the distribution of possible core radii  $r_b$  for our merger remnant by Monte Carlo sampling different SMBH spin vectors prior to SMBH binary coalescence, and using the Zlochower & Lousto (2015) relations to determine the expected recoil velocity. Our results indicate that GW recoil typically enhances the core region by a factor of 2–3 compared to the core formed through SMBH binary scouring. However, this information alone cannot be directly used to determine if GW recoil core formation has occurred in a randomly selected galaxy in the real Universe, due to the reference radius,  $r_{b,0}$ , being in general unknown.

If the core radius of a randomly selected galaxy is significantly enhanced compared to core radii for other galaxies with a similar stellar or SMBH mass, then this galaxy would be an exciting target for assessing the history of GW recoil. In Fig. 16 we plot, as a function of the remnant SMBH mass, the median core radii for each of our merger remnants and compare to the observational data presented in Thomas et al. (2016). The inferred median core sizes range from  $r_b \sim 0.5 \text{ kpc}$  for the  $v_{\text{kick}} = 0 \text{ km s}^{-1}$  simulation, to  $r_b \sim 1.4 \text{ kpc}$  for

the  $v_{\text{kick}} = 1020 \text{ km s}^{-1}$  simulation. Comparing, in Fig. 16, to the catalogue of core radii in elliptical galaxies presented in Thomas et al. (2016) as a function of SMBH mass, we find that the core radii for simulations with  $v_{\text{kick}} \lesssim 240 \text{ km s}^{-1} \simeq \sigma_{*,0}$  are consistent with the observed data to within the intrinsic scatter. For recoil velocities in excess of  $240 \text{ km s}^{-1}$ , the core radii start to become significantly offset from the data in Thomas et al. (2016). A similar conclusion is reached when comparing to the core radii data presented in Dullo & Graham (2014).

Considering that for our initial conditions, the peak in the transformation-sampled core radius distribution is in the range of 1.0–1.5 kpc (Section 4.4, depending on the assumed relation between recoil velocity and core radius), cores in the surface density profile in excess of 1.0 kpc are viable candidates for GW recoil induced core formation. Certainly galaxies hosting cores much greater than 2.0 kpc, as for example in the central galaxy A2261-BCG (Bonfini & Graham 2016; Dullo 2019), offer prime targets for SMBH recoil kicks to have been a contributing mechanism to the core formation.

Presuming that a galaxy with a large core radius has been found, assessing the magnitude of the SMBH recoil kick can be achieved with the inclusion of IFU observations of the central regions of the galaxy. As we demonstrated in Section 6.1, IFU maps uniquely allow for an observational connection to the underlying orbital structure of a galaxy, with imprints of the SMBH binary dynamics apparent in particular in the spatial distribution of  $h_4$ . Due to the removal of box orbits from the central regions of the galaxy by the SMBH binary prior to coalescence, a concentration of  $h_4 \sim 0$  appears surrounded by an annulus of  $h_4 < 0$ . We propose that identifying the inner radius of the annulus of  $h_4 < 0$  provides a tight estimate on the core radius due to binary scouring,  $r_{b,0}$ .

The appearance of  $r_{b,0}$  is particularly apparent in IFU maps restricted to just box orbits. Whilst orbital structure cannot be directly observed, but rather inferred through Schwarzschild modelling (e.g. Rix et al. 1997; Cappellari et al. 2002; Thomas et al. 2004) which introduces a new source of uncertainties, generating a model of the observed galaxy to produce mock IFU images with, analogous to the technique presented in this work, would provide a means of determining the radial extent of the annulus of  $h_4 < 0$  if it were not apparent in the observed IFU maps.

With an estimate of  $r_{b,0}$ , we are able to ascertain the relative size of the observed core radius,  $r_b/r_{b,0}$ . Assuming that a major merger has taken place to produce the observed galaxy, the GW recoil velocity can be inferred by inverting the relation between core radius and recoil velocity, as in our equation (20). Presumably this relation between  $v_{\text{kick}}$  and  $r_b$  would depend on the mass ratio of the progenitor SMBH binary, so we caution that the relations we provide are only applicable to a major merger involving two equal-mass SMBHs of  $M_{*,0} \sim 10^9 M_\odot$ . However equivalent relations may be found through a targeted parameter scan of SMBH recoil velocities, following our methods presented in Section 2.

In the event of a non-monotonic relation between recoil velocity and core radius (unlike our case, where the relation is monotonic), distinguishing the most likely  $v_{\text{kick}}$  predicted by a single value of  $r_b$  may be achieved through assessing the fraction of rosette orbits present in the Schwarzschild modelling of the observed galaxy. As demonstrated in Fig. 9, a larger  $v_{\text{kick}}$  results in less rosette orbits at the centre of the galaxy.

In this way, the SMBH recoil velocity can be well estimated with a synergy of photometric observations (to obtain  $r_b$ ), IFU observations (to determine the spatial distribution of  $h_4$ ), and potentially Schwarzschild modelling (to assess relative orbit fractions).

### 7.3 Implications for local cored galaxies

Our work has important implications for the population of local cored elliptical galaxies. For elliptical galaxies with similar stellar masses to our simulated mergers ( $M_* \sim 3 \times 10^{11} M_\odot$ ), the observed core radii are generally less than 1 kpc (e.g. Thomas et al. 2016; Dullo 2019), and the central regions of the galaxy display a tangential bias in the anisotropy parameter  $\beta$ , seen for example in the SINFONI black hole survey (Thomas et al. 2014; Saglia et al. 2016). These observations suggest that following SMBH coalescence, the typical SMBH recoil velocity is low: specifically,  $v_{\text{kick}}$  is generally less than the stellar velocity dispersion of the SMBH binary-scoured core  $\sigma_{*,0}$ . In our work, whilst the SMBH recoil velocity is set ab initio, the only physical mechanism by which it could vary is the orientation and magnitude of the SMBH binary spin vectors. Zero recoil velocity is achieved through symmetry of the SMBH binary system, and small deviations from symmetry (whether in mass or spin orientations) give rise to small recoil velocities. Consequently, our work suggests a bias towards near-aligned SMBH spin vectors, rather than SMBH spin vectors orientated randomly on the sphere. The spin vectors of an SMBH binary can evolve as a result of gas accretion and general relativistic effects.

In the case of gas-rich mergers, Miller & Krolik (2013) showed that the spin vectors of the SMBH binary are expected to align when gas accretion onto the SMBHs is prograde, and counteralign when the gas accretion is retrograde. Similar results have also been found recently by Steinle & Gerosa (2023) and Bourne et al. (2024). In the case of gas-poor mergers, SMBH binary spins likely remain isotropic until entering the GW-dominated hardening phase (e.g. Spadaro et al. 2024), with alignment later occurring through general relativistic effects, particularly in the case of unequal-mass SMBHs where the more massive SMBH spin is closely aligned with the orbital angular momentum of the binary (Berti, Kesden & Sperhake 2012). However, Sayeb et al. (2021) found that whilst general relativistic effects can cause precession of the SMBH binary spin vectors, the overall distribution of resulting recoil velocities remains relatively unaffected, owing to the dominant mechanism for SMBH binary spin alignment being the Bardeen–Peterson effect. The alignment of SMBH binary spin vectors remains an open challenge in modern astrophysics, both observationally and theoretically.

### 7.4 Modelling caveats and future work

It is worthwhile to consider the model limitations of our work, and their potential implications on our conclusions. As a first limitation, our models do not incorporate gas physics. Work by Blecha & Loeb (2008) and Blecha et al. (2011) have suggested that higher gas fractions in merger remnants can act to bring recoiling SMBHs to an equilibrium state more rapidly than in the collisionless case. For instance, following the 1 : 1 merger of two disc galaxies (leading to a total remnant baryonic mass of  $\approx 2 \times 10^{11} M_\odot$ ), Blecha et al. (2011) find that for a fixed  $v_{\text{kick}}$ , increasing progenitor disc gas fractions from 0.1 to 0.3 can decrease the maximum radius reached by the recoiling SMBH by a factor of 2–3. The inclusion of gas in these systems leads to a significant steepening of the central stellar density profile in the remnant due to merger-driven central star formation, as well as additional dynamical friction from the gas itself. While Blecha et al. (2011) consider systems with similar stellar mass to those studied here, disc-like progenitors are used as opposed to the elliptical progenitors in this work, which for a given stellar mass typically exhibit much lower gas fractions than their disc-like counterparts (e.g. Cook et al. 2019). Liao et al. (2024b) directly show

that the differences in central stellar density induced by the inclusion of gas in elliptical–elliptical mergers is negligible compared to the disc–disc case, where the authors specifically match the properties of the disc and elliptical progenitors to observed galaxies. As such, for the systems considered in this work, we do not expect gas to play a dominant role in the decay of the kicked SMBH orbit.

The inclusion of hydrodynamics may also serve to alter the stellar environment prior to SMBH binary coalescence, affecting when precisely the SMBH binary coalesces. Higher central stellar densities generally lead to more rapid coalescence of the SMBH binary through three-body interactions and a constantly-refilled loss cone (e.g. Chapon, Mayer & Teysier 2013; Souza Lima et al. 2017; Liao et al. 2024a). We thus have two time-scales to consider: the time-scale for the galaxy merger remnant to reach an equilibrium state, and the time-scale for the SMBH binary to coalesce. Most importantly, due to uncertainty in the SMBH binary merger time-scale driven by eccentricity (Nasim et al. 2020; Rawlings et al. 2023) and stellar density (Liao et al. 2024b), the triaxiality of the merger remnant at the time of SMBH coalescence is not known a priori. Additionally, AGN feedback can also alter the central triaxiality of the galaxy merger remnant, though this is a minor contribution in elliptical galaxies (Liao et al. 2024b). A varying triaxiality may impact the asymmetric torquing of the recoiling SMBH, affecting the frequency and timing of the SMBH passages through the stellar core. Consequently, this might in principle alter the size of the core radius of the merger remnant once the SMBH has settled. However, as demonstrated in Fig. 1 and discussed in Section 3.3, the passages of the SMBH through the stellar core occur when the SMBH trajectory is predominantly radial, despite a low degree of triaxiality being present in the central regions of the merger remnant at the time of coalescence. Thus, we do not expect the number of oscillations required for the kicked SMBH to settle to depend strongly on the triaxiality, however the time required for the SMBH to settle may show some variation. From the analysis of the Lagrangian radii, the later stages of the stellar core growth occur during the passages of the SMBH that take it through the core, and not the total time for the SMBH to settle, thus we expect our results to be robust against triaxiality variation.

In this work, we have only explored one set of initial conditions, and not considered differing mass ratios of progenitor galaxies or SMBHs, nor different stellar density profiles. Additionally, we consider only a single generation of galaxy mergers, whereas in the cosmological context multiple generations of mergers are expected to have occurred, particularly for massive systems such as the ones we discuss (e.g. Bezanson et al. 2009; Naab et al. 2009; Feldmann et al. 2010; van Dokkum et al. 2015; Rantala et al. 2024). Whilst exploring the full parameter space is beyond the scope of this work, we may consider the results of Khonji et al. (2024), who found that there was no clear trend between SMBH mass and core size from GW recoil, provided the SMBH settled following its initial ejection. From their work, we can infer that for recoil velocities above  $v_{\text{kick}} \gtrsim 0.5v_{\text{esc}}$ , the choice of initial conditions does not significantly affect the final core size: this is in contrast to the core size due to binary scouring, which increases with increasing SMBH mass. The sensitivity of the core size to initial conditions for recoil velocities  $v_{\text{kick}} \lesssim 0.5v_{\text{esc}}$  remains to be explored. One could, for example, use the methodology developed here and apply it to a statistically significant sample of galaxy mergers from cosmological simulations, to investigate the choice of merger initial conditions. In particular, a statistically significant sample would require both a large number of galaxy mergers, and a representative, diverse sample of galaxy mergers with an occurrence frequency consistent with cosmology. Such an investigation would

not only help address the first limitation raised above, but also answer a new question: what is the overall distribution of core radii in the Universe?

Finally, we make use of the Zlochower & Lousto (2015) relations to determine the SMBH recoil velocity from the pre-merger SMBH binary configuration, which are derived from numerical relativity simulations. As part of the modelling in this work, we assume that the distribution of spin magnitude  $\alpha_*$  at the separation of a binary merger in KETJU (some  $12 R_s$ , where  $R_s$  is the Schwarzschild radius of the combined SMBH binary mass) is consistent with the distribution arrived at from numerical relativity, which is necessarily resolved to much smaller scales than our simulations. Whilst using a different relation than that presented in Zlochower & Lousto (2015) would not affect the kinematic analysis nor the derived relation between recoil velocity and core radius, the distribution of core radii (Fig. 8) would change. A distribution of core radii derived from the method proposed in the third limitation discussed would also be sensitive to this.

## 8 CONCLUSIONS

In conclusion, we find that the GW-induced recoil of an SMBH in a massive elliptical galaxy leaves distinct signatures that would be observable in the real Universe. Specifically, we find:

- (i) Asymmetric torques on the recoiling SMBH can alter the SMBH trajectory, potentially delaying stellar core growth by repeated passages of the settling SMBH until the SMBH passes through the core.
- (ii) A core is not present in the 3D stellar density profile unless the SMBH has been ejected entirely from the galaxy, corresponding to the case of zero oscillations of the kicked SMBH about the galaxy centre.
- (iii) A higher recoil velocity induces a larger core in the projected stellar mass density of the merger remnant than lower recoil velocities, with our models indicating that core radii exceeding 1 kpc are not only possible, but likely. As a consequence, the mass deficit due to SMBH recoil increases with larger recoil velocity, up to  $\sim 90$  per cent of the coalesced SMBH mass.
- (iv) For merger remnants with  $v_{\text{kick}} \lesssim \sigma_{*,0}$ , the majority of stellar mass within the core has angular momentum-conserving orbits. For recoil velocities above this threshold, box orbits which do not conserve angular momentum dominate the mass budget.
- (v) Similarly, merger remnants with  $v_{\text{kick}} \gtrsim \sigma_{*,0}$  are ergodic within the core, with  $\beta \sim 0$ . Only for the lowest kick velocities are tangentially biased cores observed, suggesting that the majority of local cored galaxies do not have an SMBH which has experienced a large recoil velocity.
- (vi) In kinematic observations of the inner region of the merger remnant, the core due solely to SMBH binary scouring, without a contribution from SMBH recoil, can be estimated by identifying the inner radius when the LOSVD symmetric deviation parameter  $h_4$  decreases to  $h_4 < 0$ . This in principle allows for an estimate of  $v_{\text{kick}}$  from the observed core radius.

Taken together, this work establishes a causal link between forward-modelled observations of a galaxy merger remnant – both photometric and kinematic – with the complex physics underlying SMBH binary mergers, and their associated GW-induced recoil kicks. In the future, this will allow us to quantify the recoil velocity of SMBHs in observations of major mergers, opening the way for tighter constraints to be placed on the SMBH binary merger process, particularly for those galaxies in the local Universe.

## ACKNOWLEDGEMENTS

We thank the anonymous referee for their comments which helped improve the manuscript. We also thank Jens Thomas for useful discussions on IFU observations and Aki Vehtari for helpful discussions on Bayesian modelling techniques. AR acknowledges the support by the University of Helsinki Research Foundation. AR, AK, MM, RJW, and PHJ acknowledge the support by the European Research Council via ERC Consolidator Grant KETJU (no. 818930). MM and PHJ acknowledge the support of the Academy of Finland grant 339127. RJW acknowledges the support of the Forrest Research Foundation. NK acknowledges support of the Research Council of Finland Flagship programme: Finnish Center for Artificial Intelligence and the Finnish Foundation for Technology Promotion. SL acknowledges the supports by the National Natural Science Foundation of China (NSFC) grant (no. 12473015, 11988101) and the K. C. Wong Education Foundation. TN acknowledges support from the Deutsche Forschungsgemeinschaft (DFG, German Research Foundation) under Germany's Excellence Strategy–EXC-2094 – 390 783 311 from the DFG Cluster of Excellence ‘ORIGINS’.

The numerical simulations used computational resources provided by the CSC—IT centre for Science, Finland.

We list here the roles and contributions of the authors according to the Contributor Roles Taxonomy (CRediT). **AR**: conceptualization, methodology, formal analysis, investigation, data curation, writing: original. **AK**: formal analysis, writing: original. **MM**: formal analysis, writing: original. **SS**: formal analysis, writing: original. **RJW**: investigation, writing: original. **NK**: methodology, writing: original. **SL**: conceptualisation, writing: review. **AR**: writing: review. **PHJ**: supervision, writing: original, funding acquisition. **TN**: conceptualisation, writing: review. **DI**: writing: review.

KETJU (Rantala et al. 2017; Mannerkoski et al. 2023), GADGET-4 (Springel et al. 2021), NUMPY (Harris et al. 2020), SCIPY (Virtanen et al. 2020), MATPLOTLIB (Hunter 2007), PYGAD (Röttgers et al. 2020), STAN (Stan Development Team 2018), CMDSTANPY (Stan Development Team 2018), ARVIZ (Kumar et al. 2019), SEABORN (Waskom 2021).

## DATA AVAILABILITY

The data underlying this article will be shared on reasonable request to the corresponding author.

## REFERENCES

Agazie G. et al., 2023, *ApJ*, 951, L8  
 Amaro-Seoane P. et al., 2023, *Living Rev. Relat.*, 26, 2  
 Bailin J., Steinmetz M., 2005, *ApJ*, 627, 647  
 Barnes J. E., Hernquist L., 1996, *ApJ*, 471, 115  
 Barrows R. S., Comerford J. M., Greene J. E., Pooley D., 2016, *ApJ*, 829, 37  
 Batcheldor D., Robinson A., Axon D. J., Perlman E. S., Merritt D., 2010, *ApJ*, 717, L6  
 Begelman M. C., Blandford R. D., Rees M. J., 1980, *Nature*, 287, 307  
 Bekenstein J. D., 1973, *ApJ*, 183, 657  
 Berzik P., Merritt D., Spurzem R., Bischof H.-P., 2006, *ApJ*, 642, L21  
 Berti E., Kesden M., Sperhake U., 2012, *Phys. Rev. D*, 85, 124049  
 Bezanson R., van Dokkum P. G., Tal T., Marchesini D., Kriek M., Franx M., Coppi P., 2009, *ApJ*, 697, 1290  
 Binney J., Tremaine S., 2008, *Galactic Dynamics: Second Edition*. Princeton Univ. Press, Princeton  
 Blanchet L., 2014, *Living Rev. Relat.*, 17, 2  
 Blecha L., Loeb A., 2008, *MNRAS*, 390, 1311  
 Blecha L., Cox T. J., Loeb A., Hernquist L., 2011, *MNRAS*, 412, 2154  
 Bonfini P., Graham A. W., 2016, *ApJ*, 829, 81

Bourne M. A., Fiacconi D., Sijacki D., Piotrowska J. M., Koudmani S., 2024, *MNRAS*, 534, 3448  
 Boylan-Kolchin M., Ma C.-P., Quataert E., 2004, *ApJ*, 613, L37  
 Campanelli M., Lousto C., Zlochower Y., Merritt D., 2007, *ApJ*, 659, L5  
 Cannarozzo C. et al., 2023, *MNRAS*, 520, 5651  
 Cappellari M., 2016, *ARA&A*, 54, 597  
 Cappellari M., Copin Y., 2003, *MNRAS*, 342, 345  
 Cappellari M., Verolme E. K., van der Marel R. P., Verdoes Kleijn G. A., Illingworth G. D., Franx M., Carollo C. M., de Zeeuw P. T., 2002, *ApJ*, 578, 787  
 Cappellari M. et al., 2007, *MNRAS*, 379, 418  
 Chandrasekhar S., 1943, *ApJ*, 97, 255  
 Chapon D., Mayer L., Teyssier R., 2013, *MNRAS*, 429, 3114  
 Comerford J. M., Greene J. E., 2014, *ApJ*, 789, 112  
 Cook R. H. W., Cortese L., Catinella B., Robotham A., 2019, *MNRAS*, 490, 4060  
 Dehnen W., 2005, *MNRAS*, 360, 892  
 van Dokkum P. G. et al., 2015, *ApJ*, 813, 23  
 van Dokkum P. et al., 2023, *ApJ*, 946, L50  
 Dosopoulou F., Greene J. E., Ma C.-P., 2021, *ApJ*, 922, 40  
 Dullo B. T., 2019, *ApJ*, 886, 80  
 Dullo B. T., Graham A. W., 2014, *MNRAS*, 444, 2700  
 EPTA Collaboration, 2024, *A&A*, 685, A94  
 Ebrova I., Łokas E. L., 2017, *ApJ*, 850, 144  
 Emsellem E. et al., 2007, *MNRAS*, 379, 401  
 Faber S. M. et al., 1997, *AJ*, 114, 1771  
 Feldmann R., Carollo C. M., Mayer L., Renzini A., Lake G., Quinn T., Stinson G. S., Yepes G., 2010, *ApJ*, 709, 218  
 Ferrarese L., van den Bosch F. C., Ford H. C., Jaffe W., O’Connell R. W., 1994, *AJ*, 108, 1598  
 Förster Schreiber N. M., Wuyts S., 2020, *ARA&A*, 58, 661  
 Franx M., Illingworth G., de Zeeuw T., 1991, *ApJ*, 383, 112  
 Frigo M., Naab T., Rantala A., Johansson P. H., Neureiter B., Thomas J., Rizzuto F., 2021, *MNRAS*, 508, 4610  
 Gabry J., Simpson D., Vehtari A., Betancourt M., Gelman A., 2019, *J. R. Stat. Soc. Ser. A*, 182, 389  
 Gelman A., Hwang J., Vehtari A., 2014, *Stat. Comput.*, 24, 997  
 Gelman A., Carlin J. B., Stern H. S., Dunson D. B., Vehtari A., Rubin D. B., 2015, *Bayesian Data Analysis, 3rd edn*. Chapman and Hall/CRC, Boca Raton  
 Genina A., Springel V., Rantala A., 2024, *MNRAS*, 534, 957  
 Gerhard O. E., 1983, *MNRAS*, 203, 19P  
 González-García A. C., Oñorbe J., Domínguez-Tenreiro R., Gómez-Flechoso M. A., 2009, *A&A*, 497, 35  
 González J. A., Sperhake U., Brüggemann B., Hannam M., Husa S., 2007a, *Phys. Rev. Lett.*, 98, 091101  
 González J. A., Hannam M., Sperhake U., Brüggemann B., Husa S., 2007b, *Phys. Rev. Lett.*, 98, 231101  
 Graham A. W., Erwin P., Trujillo I., Asensio Ramos A., 2003, *AJ*, 125, 2951  
 Grissom R. J., Kim J. J., 2001, *Psychol. Methods*, 6, 135  
 Gualandris A., Merritt D., 2008, *ApJ*, 678, 780  
 Gualandris A., Read J. I., Dehnen W., Bortolas E., 2017, *MNRAS*, 464, 2301  
 Häring N., Rix H.-W., 2004, *ApJ*, 604, L89  
 Harris C. R. et al., 2020, *Nature*, 585, 357  
 Hernquist L., 1990, *ApJ*, 356, 359  
 Hernquist L., Ostriker J. P., 1992, *ApJ*, 386, 375  
 Hills J. G., 1983, *AJ*, 88, 1269  
 Hills J. G., Fullerton L. W., 1980, *AJ*, 85, 1281  
 Hilz M., Naab T., Ostriker J. P., Thomas J., Burkert A., Jesseit R., 2012, *MNRAS*, 425, 3119  
 Hogg J. D., Blecha L., Reynolds C. S., Smith K. L., Winter L. M., 2021, *MNRAS*, 503, 1688  
 Holley-Bockelmann K., Sigurdsson S., 2006, preprint (arXiv:astro-ph/0601520)  
 Hopkins P. F., Cox T. J., Dutta S. N., Hernquist L., Kormendy J., Lauer T. R., 2009a, *ApJS*, 181, 135  
 Hopkins P. F., Lauer T. R., Cox T. J., Hernquist L., Kormendy J., 2009b, *ApJS*, 181, 486

- Hunter J. D., 2007, *Comput. Sci. Eng.*, 9, 90
- Jesseit R., Naab T., Burkert A., 2005, *MNRAS*, 360, 1185
- Johansson P. H., Naab T., Burkert A., 2009, *ApJ*, 690, 802
- Johansson P. H., Naab T., Ostriker J. P., 2012, *ApJ*, 754, 115
- Kallioinen N., Paananen T., Bürkner P.-C., Vehtari A., 2024, *Stat. Comput.*, 34, 57
- Karl S. J., Aarseth S. J., Naab T., Haehnelt M. G., Spurzem R., 2015, *MNRAS*, 452, 2337
- Khochfar S., Burkert A., 2006, *A&A*, 445, 403
- Khonji N., Gualandris A., Read J. I., Dehnen W., 2024, *ApJ*, 974, 204
- Kim D. C., Yoon I., Prigon G. C., Evans A. S., Harvey D., Stierwalt S., Kim J. H., 2017, *ApJ*, 840, 71
- Komossa S., Zhou H., Lu H., 2008, *ApJ*, 678, L81
- Kormendy J., 1984, *ApJ*, 287, 577
- Kormendy J., Bender R., 1996, *ApJ*, 464, L119
- Kormendy J., Ho L. C., 2013, *ARA&A*, 51, 511
- Kormendy J., Fisher D. B., Cornell M. E., Bender R., 2009, *ApJS*, 182, 216
- Koss M. et al., 2014, *MNRAS*, 445, 515
- Krajnović D. et al., 2011, *MNRAS*, 414, 2923
- Kumar R., Carroll C., Hartikainen A., Martin O., 2019, *J. Open Source Softw.*, 4, 1143
- Lagos C. d. P., Emsellem E., van de Sande J., Harborne K. E., Cortese L., Davison T., Foster C., Wright R. J., 2022, *MNRAS*, 509, 4372
- Lahén N., Johansson P. H., Rantala A., Naab T., Frigo M., 2018, *MNRAS*, 475, 3934
- Lauer T. R., 1983, PhD thesis, University of California, Santa Cruz
- Lauer T. R., 1985, *ApJ*, 292, 104
- Lena D., Robinson A., Marconi A., Axon D. J., Capetti A., Merritt D., Batcheldor D., 2014, *ApJ*, 795, 146
- Liao S., Irodotou D., Johansson P. H., Naab T., Rizzuto F. P., Hislop J. M., Rawlings A., Wright R. J., 2024a, *MNRAS*, 528, 5080
- Liao S., Irodotou D., Johansson P. H., Naab T., Rizzuto F. P., Hislop J. M., Wright R. J., Rawlings A., 2024b, *MNRAS*, 530, 4058
- Madau P., Quataert E., 2004, *ApJ*, 606, L17
- Mannerkoski M., Johansson P. H., Rantala A., Naab T., Liao S., Rawlings A., 2022, *ApJ*, 929, 167
- Mannerkoski M., Rawlings A., Johansson P. H., Naab T., Rantala A., Springel V., Irodotou D., Liao S., 2023, *MNRAS*, 524, 4062
- Mehrgan K., Thomas J., Saglia R., Parikh T., Bender R., 2023, *ApJ*, 948, 79
- Merritt D., 2006, *ApJ*, 648, 976
- Merritt D., 2013, *Dynamics and Evolution of Galactic Nuclei*. Princeton Univ. Press, Princeton
- Merritt D., Milosavljević M., 2005, *Living Rev. Relat.*, 8, 8
- Merritt D., Vasiliev E., 2011, *ApJ*, 726, 61
- Merritt D., Milosavljević M., Favata M., Hughes S. A., Holz D. E., 2004, *ApJ*, 607, L9
- Merritt D., Berczik P., Laun F., 2007, *AJ*, 133, 553
- Miller M. C., Krolik J. H., 2013, *ApJ*, 774, 43
- Milosavljević M., Merritt D., 2001, *ApJ*, 563, 34
- Naab T., Burkert A., 2003, *ApJ*, 597, 893
- Naab T., Ostriker J. P., 2017, *ARA&A*, 55, 59
- Naab T., Johansson P. H., Ostriker J. P., 2009, *ApJ*, 699, L178
- Naab T. et al., 2014, *MNRAS*, 444, 3357
- Nakano T., Makino J., 1999, *ApJ*, 510, 155
- Nasim I., Gualandris A., Read J., Dehnen W., Delorme M., Antonini F., 2020, *MNRAS*, 497, 739
- Nasim I. T., Gualandris A., Read J. I., Antonini F., Dehnen W., Delorme M., 2021, *MNRAS*, 502, 4794
- Neureiter B. et al., 2021, *MNRAS*, 500, 1437
- Neureiter B., Thomas J., Rantala A., Naab T., Mehrgan K., Saglia R., de Nicola S., Bender R., 2023, *ApJ*, 950, 15
- Oser L., Ostriker J. P., Naab T., Johansson P. H., Burkert A., 2010, *ApJ*, 725, 2312
- Partmann C., Naab T., Rantala A., Genina A., Mannerkoski M., Johansson P. H., 2024, *MNRAS*, 532, 4681
- Pesce D. W., Braatz J. A., Condon J. J., Greene J. E., 2018, *ApJ*, 863, 149
- Pesce D. W., Seth A. C., Greene J. E., Braatz J. A., Condon J. J., Kent B. R., Krajnović D., 2021, *ApJ*, 909, 141
- Peters P. C., 1964, *Phys. Rev.*, 136, 1224
- Peters P. C., Mathews J., 1963, *Phys. Rev.*, 131, 435
- Postman M. et al., 2012, *ApJ*, 756, 159
- Power C., Navarro J. F., Jenkins A., Frenk C. S., White S. D. M., Springel V., Stadel J., Quinn T., 2003, *MNRAS*, 338, 14
- Prugniel P., Simien F., 1997, *A&A*, 321, 111
- Qu Y. et al., 2017, *MNRAS*, 464, 1659
- Quenneville M. E., Blakeslee J. P., Ma C.-P., Greene J. E., Gwyn S. D. J., Ciccone S., Nyiri B., 2024, *MNRAS*, 527, 249
- Quinlan G. D., 1996, *New Astron.*, 1, 35
- Quinlan G. D., Hernquist L., 1997, *New Astron.*, 2, 533
- Rantala A., Pihajoki P., Johansson P. H., Naab T., Lahén N., Sawala T., 2017, *ApJ*, 840, 53
- Rantala A., Johansson P. H., Naab T., Thomas J., Frigo M., 2018, *ApJ*, 864, 113
- Rantala A., Johansson P. H., Naab T., Thomas J., Frigo M., 2019, *ApJ*, 872, L17
- Rantala A., Pihajoki P., Mannerkoski M., Johansson P. H., Naab T., 2020, *MNRAS*, 492, 4131
- Rantala A., Rawlings A., Naab T., Thomas J., Johansson P. H., 2024, *MNRAS*, 535, 1202
- Rawlings A., Mannerkoski M., Johansson P. H., Naab T., 2023, *MNRAS*, 526, 2688
- Riha A. E., Siccha N., Oulasvirta A., Vehtari A., 2024, preprint (arXiv:2404.01688)
- Rix H.-W., de Zeeuw P. T., Cretton N., van der Marel R. P., Carollo C. M., 1997, *ApJ*, 488, 702
- Rodríguez-Gomez V. et al., 2016, *MNRAS*, 458, 2371
- Röttgers B., Naab T., Oser L., 2014, *MNRAS*, 445, 1065
- Röttgers B., Naab T., Cernetic M., Davé R., Kauffmann G., Borthakur S., Foidl H., 2020, *MNRAS*, 496, 152
- Rusli S. P., Erwin P., Saglia R. P., Thomas J., Fabricius M., Bender R., Nowak N., 2013, *AJ*, 146, 160
- Saglia R. P. et al., 2016, *ApJ*, 818, 47
- Sahu N., Graham A. W., Davis B. L., 2020, *ApJ*, 903, 97
- Santucci G. et al., 2022, *ApJ*, 930, 153
- Santucci G. et al., 2023, *MNRAS*, 521, 2671
- Santucci G. et al., 2024, *MNRAS*, 534, 502
- Sayeb M., Blecha L., Kelley L. Z., Gerosa D., Kesden M., Thomas J., 2021, *MNRAS*, 501, 2531
- Sérsic J. L., 1963, *Bol. Asoc. Argentina Astron. La Plata Argentina*, 6, 41
- Sérsic J. L., 1968, *Atlas de Galaxias Australes*. Observatorio Astronomico, Cordoba, Argentina
- Skipper C. J., Browne I. W. A., 2018, *MNRAS*, 475, 5179
- Souza Lima R., Mayer L., Capelo P. R., Bellovary J. M., 2017, *ApJ*, 838, 13
- Spadaro A., Buscicchio R., Izquierdo-Villalba D., Gerosa D., Klein A., Pratten G., 2024, *Phys. Rev. D*, 111, 023004
- Springel V., Pakmor R., Zier O., Reinecke M., 2021, *MNRAS*, 506, 2871
- Stan Development Team, 2018, *The Stan Core Library*, available at: <http://mc-stan.org/8>
- Steinhardt C. L. et al., 2012, *ApJ*, 759, 24
- Steinle N., Gerosa D., 2023, *MNRAS*, 519, 5031
- Thomas J., Saglia R. P., Bender R., Thomas D., Gebhardt K., Magorrian J., Richstone D., 2004, *MNRAS*, 353, 391
- Thomas J., Saglia R. P., Bender R., Erwin P., Fabricius M., 2014, *ApJ*, 782, 39
- Thomas J., Ma C.-P., McConnell N. J., Greene J. E., Blakeslee J. P., Janish R., 2016, *Nature*, 532, 340
- Tichy W., Marronetti P., 2007, *Phys. Rev. D*, 76, 061502
- Vasiliev E., Antonini F., Merritt D., 2015, *ApJ*, 810, 49
- Vehtari A., Gelman A., Gabry J., 2017, *Stat. Comput.*, 27, 1413
- Vehtari A., Gelman A., Simpson D., Carpenter B., Bürkner P.-C., 2021, *Bayesian Anal.*, 16, 667
- Vehtari A., Simpson D., Gelman A., Yao Y., Gabry J., 2024, *J. Mach. Learn. Res.*, 25, 1
- Virtanen P. et al., 2020, *Nat. Methods*, 17, 261
- Volonteri M., 2007, *ApJ*, 663, L5



Waskom M. L., 2021, *J. Open Source Softw.*, 6, 3021  
 Wellons S. et al., 2015, *MNRAS*, 449, 361  
 Xu H. et al., 2023, *Res. Astron. Astrophys.*, 23, 075024  
 Zic A. et al., 2023, *Publ. Astron. Soc. Aust.*, 40, e049  
 Zlochower Y., Lousto C. O., 2015, *Phys. Rev. D*, 92, 024022  
 van den Bosch R. C. E., 2016, *ApJ*, 831, 134  
 van der Marel R. P., Franx M., 1993, *ApJ*, 407, 525

## APPENDIX A: TRIAXIALITY

To assess the impact of our (arbitrarily) chosen direction in which the SMBH recoil velocity is applied, we calculate the triaxiality of all merger remnants at the time when the SMBH has settled.

We take all stellar particles within a fraction of the virial radius  $r_{200}$ , defined as the radius at which the mean density is equal to 200 times greater than the critical density; the virial radius is  $\sim 450$  kpc for the merger remnants in this study.

We determine the ratios  $b/a$  and  $c/a$ , where  $a$ ,  $b$ , and  $c$  are the eigenvalues of the reduced inertia tensor (Gerhard 1983; Bailin &

Steinmetz 2005):

$$\tilde{I}_{\text{red}} = \sum_k \frac{r_{k,i} r_{k,j}}{r_k^2}, \quad (\text{A1})$$

and  $c \leq b \leq a$ . The tensor  $\tilde{I}_{\text{red}}$  is determined by binning the stellar component of the remnant into 20 radial shells from  $10^{-3}r_{200}$  to  $10^{-1}r_{200}$ : the binning of particles is not cumulative. We apply a uniform filter to reduce Poisson noise due to low particle numbers at small radii. The radial variations of the ratios  $b/a$  and  $c/a$  are plotted in Fig. A1 in the top and middle panels, respectively. The merger remnants display mildly triaxial cores, albeit without dependence on the recoiling SMBH velocity. At radii greater than 4 kpc, the triaxiality of the merger remnants is consistent. Importantly, the  $v_{\text{kick}} = 0$ ,  $\text{km s}^{-1}$  case also displays only minor variation in  $b/a$  and  $c/a$  with radius: as this is a good proxy for the pre-merger galaxy remnant, we do not expect triaxiality to dominate over the recoil velocity in the motion of the settling SMBH.

To quantify the nature of the merger remnant triaxiality as a function of radius, we also compute the triaxiality parameter  $T$ :

$$T = \frac{1 - (b/a)^2}{1 - (c/a)^2} \quad (\text{A2})$$

following Franx, Illingworth & de Zeeuw (1991). Values of  $T$  approaching 1 indicate a prolate system, and values of  $T$  approaching 0 indicate an oblate system. As seen in the bottom panel of Fig. A1, at radii  $r \gtrsim 5$  kpc all merger remnants are prolate systems. For radii  $r \lesssim 5$  kpc, only the  $v_{\text{kick}} = 1020$   $\text{km s}^{-1}$  merger remnant tends to an oblate system.

## APPENDIX B: CORE-SÉRSIC FIT PARAMETER ESTIMATES

We use a Bayesian hierarchical model to determine the posterior distributions for the core-Sérsic projected mass density profile equation (12). Bayesian inference, in its simplest form, aims to infer the distribution of the parameter  $\theta$  in some model that describe data  $y$ : this is done with Bayes' formula:

$$p(\theta|y) \propto p(\theta)\mathcal{L}(y|\theta), \quad (\text{B1})$$

where  $p(\theta|y)$  is the posterior distribution,  $p(\theta)$  is the prior distribution that encodes belief about how the parameter  $\theta$  is distributed, and  $\mathcal{L}(y|\theta)$  is the likelihood of observing the data  $y$  given the model parameter  $\theta$ . In the case that there are groups of data that are subsets of some global population, and these subsets are exchangeable in the sense that there is no distinguishing order to them, we can model each subset of data  $y_j$  as having its own value of the model parameter  $\theta_j$ . The distribution of all values of  $\theta_j$  can then be modelled as samples from a global distribution, termed a hyperdistribution, with hyperparameter(s)  $\phi$ : this is where the hierarchical nature of the model is introduced. A prior distribution can then be assigned to the hyperparameter  $\phi$ ,  $p(\phi)$ . As such, equation (B1) then takes the form:

$$p(\theta, \phi|y) \propto p(\phi)p(\theta|\phi)\mathcal{L}(y|\theta, \phi). \quad (\text{B2})$$

In our application of inferring the parameter vector  $\theta \equiv [r_b, \Sigma_b, \gamma, R_e, n, \alpha]$  that describes the projected stellar mass density profile of the galaxy merger remnant, each projection from which the merger remnant is viewed from constitutes a subset of the surface density data  $\Sigma_j$ . As each of the projections are unordered and exchangeable (i.e. there is no distinguishing label for the projections), and each projection is of the same merger remnant, the hierarchical model naturally lends itself. For each projection, we thus infer the

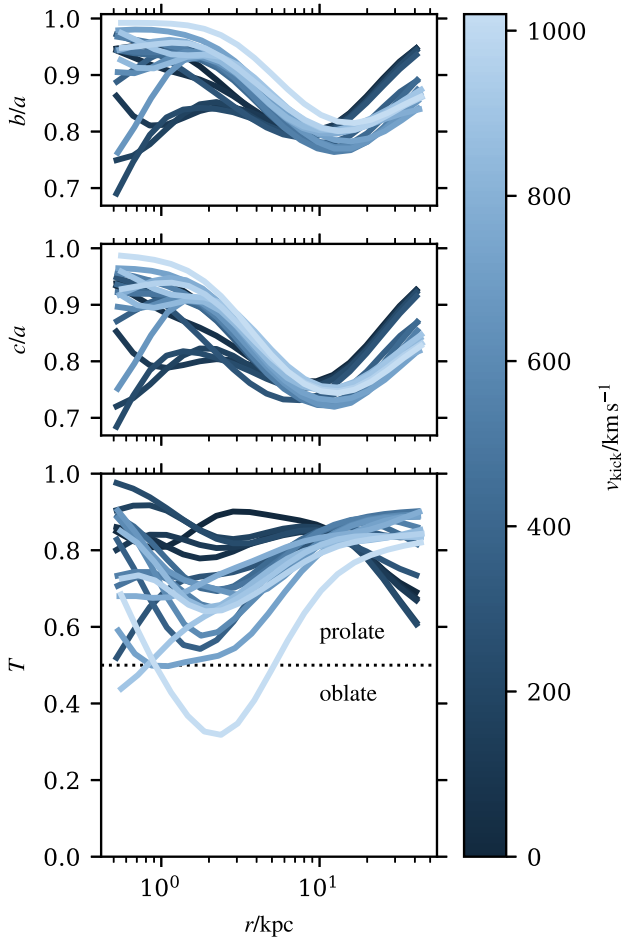


**Figure A1.** Triaxiality ratios  $b/a$  and  $c/a$  as a function of radius for all merger remnants in the analysis in the top panel and middle panel, respectively. Lines are colour coded by the kick velocity, with the same scheme as in Fig. 4. Note that the  $v_{\text{kick}} = 0$   $\text{km s}^{-1}$  case is equivalent to the pre-merger remnant. In the bottom panel, the variation of the triaxiality parameter  $T$  is shown as a function of radius: the merger remnants in this study are predominantly prolate systems.

six parameters of  $\theta$ , and assume that these values are drawn from a common, global distribution of all possible  $\theta$  vectors. Hence, we are effectively inferring the global hyperparameters  $\theta^{\text{hyp}}$  that describe the latent parameters  $\theta$  that we are interested in. This idea is demonstrated in the directed acyclic graph (DAG) for the model, shown in Fig. 5. The posterior density can thus be constructed for each projection- and radially dependent surface density element  $\Sigma_{i,j}^L \equiv \log_{10}(\Sigma_{i,j})$  as:

$$p(\theta, \theta^{\text{hyp}} | \Sigma'_{i,j}) \propto p(\theta^{\text{hyp}}) p(\theta | \theta^{\text{hyp}}) \times \prod_j^{N_{\text{proj}}} \prod_i^{N_R} \mathcal{N}(\Sigma_{i,j}^L | \hat{\Sigma}^L(R_i | \theta_j, \theta^{\text{hyp}}), \tau_i), \quad (\text{B3})$$

where we use a normal distribution<sup>8</sup> as the likelihood function, and the error in the fit depends on the radial bin  $i$ .

We use weakly constrained prior distributions for each of the hyperparameters in  $\theta^{\text{hyp}}$ , where these prior distributions are chosen to reflect reasonable values (Gabry et al. 2019) that the parameters may take (e.g. distributions of a radial quantity are chosen so as to be positively constrained). The distributions of the hyperparameters are given in Table 1.

We fit the model with STAN (Stan Development Team 2018) using the No U-turn sampler [NUTS, a variant of Hamiltonian Monte Carlo (HMC)] with four chains each of 4000 iterations, of which the first 2000 are discarded as warmup. This resulted in 8000 draws from the posterior distribution of  $\theta$ , whereby we ensure the quality of the HMC fit by enforcing a diagnostic value  $\hat{R}$  (comparison of between-chain and within-chain variance) less than 1.05, the effective sample size is high, and that the number of divergent transitions is less than 5 per cent (for details see Stan Development Team 2018; Vehtari et al. 2021). We perform additional prior sensitivity tests using the power-scaling method described in Kallioinen et al. (2024), ensuring that the sensitivity diagnostic for prior power-scaling is less than 0.05 for the latent parameters  $\theta$  of the model. This recommended threshold indicates that the sampled posterior distributions of the latent parameters are not sensitive to the particular prior distributions used.

In Fig. B1, we show as box plots the distributions of the six latent parameters in the core-Sérsic profile, equation (12). The dark bars indicate the median of each distribution, and the boxes are bounded at the bottom by the 25th percentile, and capped at the 75th percentile. As discussed in the main text, the median core radius  $r_b$  (top left) increases in both magnitude and variance with increasing kick velocity. The density at the core radius (top left) decreases with increasing kick velocity, as well as having a variance which is largely independent of the kick velocity. The slope of the inner density profile,  $\gamma$  (centre left) is largely independent of the kick velocity, as is the effective radius of the galaxy (centre right) and transition index (bottom left). The Sérsic index (bottom right) is constant for  $v_{\text{kick}} \leq 300 \text{ km s}^{-1}$ , and is constant, albeit

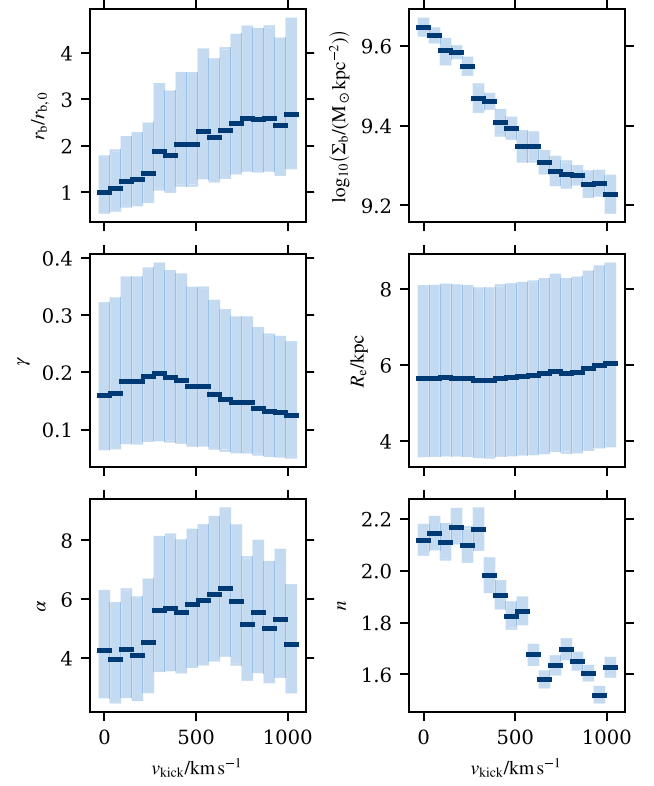


**Figure B1.** Box plots of the six parameters in the core-Sérsic model (from top left to bottom right) as a function of the kick velocity: the core radius normalized to the pre-merger core radius  $r_b/r_{b,0}$ , the density at the core radius  $\log_{10} \Sigma_b$ , the core slope  $\gamma$ , the effective radius  $R_e$ , the profile transition index  $\alpha$ , and the Sérsic index  $n$ .

with a smaller value, for  $v_{\text{kick}} \geq 660 \text{ km s}^{-1}$ . For the intermediate kick velocities, there appears to be a linear decrease in the Sérsic index  $n$ .

The joint relation between the latent parameters in equation (12) can be seen in the representative example of  $v_{\text{kick}} = 600 \text{ km s}^{-1}$  in Fig. B2. The leading diagonal shows the marginal distributions of each latent parameter; each distribution is unimodal. The contours in the lower diagonal triangle show the joint posterior distribution between each of the latent parameters in equation (12), with the contour colouring indicating various highest density intervals (HDIs). In no pairing of parameters is a strong covariance observed; the marginal distributions are orthogonal to each other. One case worth a special mention is the width of the 25 per cent HDI for the parameter  $\alpha$ . The wide HDI indicates that a large range of  $\alpha$  values maximize the posterior distribution. However, as discussed in Graham et al. (2003), values of  $\alpha \gtrsim 3$  have a similar effect to induce a sharp transition between the inner and outer surface density profiles. The variation of  $\alpha$ , particularly to large values greater than 10, are not expected to have a strong effect on the overall surface density profile.

<sup>8</sup>Note that the normal distributions  $\mathcal{N}$  are parametrized using the standard deviation  $\sigma$  in this work, as opposed to the variance  $\sigma^2$  as is common in many statistics references.

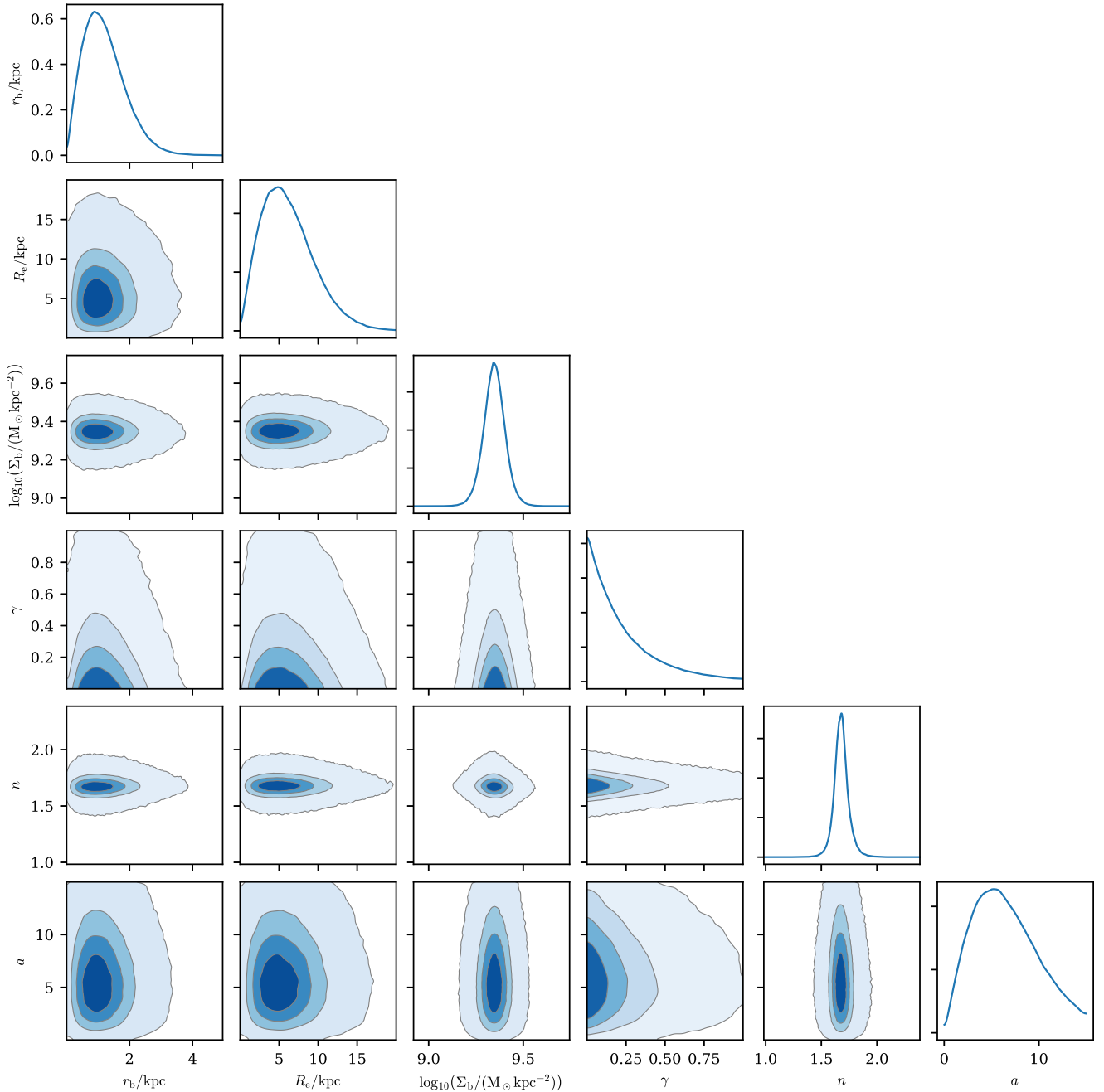


**Figure B2.** Corner plot of the latent parameters in the core-Sérsic model for a representative example, here the  $v_{\text{kick}} = 600 \text{ km s}^{-1}$  instance. Contours indicate, from dark to light blue, the 25 per cent, 50 per cent, 75 per cent, and 99 per cent highest density intervals (HDIs). All distributions are unimodal with little cross-correlation between the latent variables.

### APPENDIX C: SUPPORTING INFORMATION FOR IFU ANALYSIS

In Fig. C1, we show, for each recoil velocity, kernel density estimates of the apocentre distributions for stellar particles within a mean position of  $0.25r_{1/2}$  from the merger remnant centre. The distributions are clearly left-skewed, and becoming increasingly skewed as the recoil velocity increases, with the exception of the  $v_{\text{kick}} = 2000 \text{ km s}^{-1}$  simulation, as discussed in the main text.

In Fig. C2, we show how the radial dependence of  $\langle h_4 \rangle$  varies with regard to the time when the SMBH has settled, defined  $t - t_{\text{settle}} = 0 \text{ Gyr}$ , for a representative example ( $v_{\text{kick}} = 900 \text{ km s}^{-1}$ ). At the time the SMBH settled, and times following this point, the radial dependence of  $\langle h_4 \rangle$  is time-invariant, for both the parallel and orthogonal projections. This ensures that our conclusions in the main text are not sensitive to the exact moment the LOSVD is constructed.

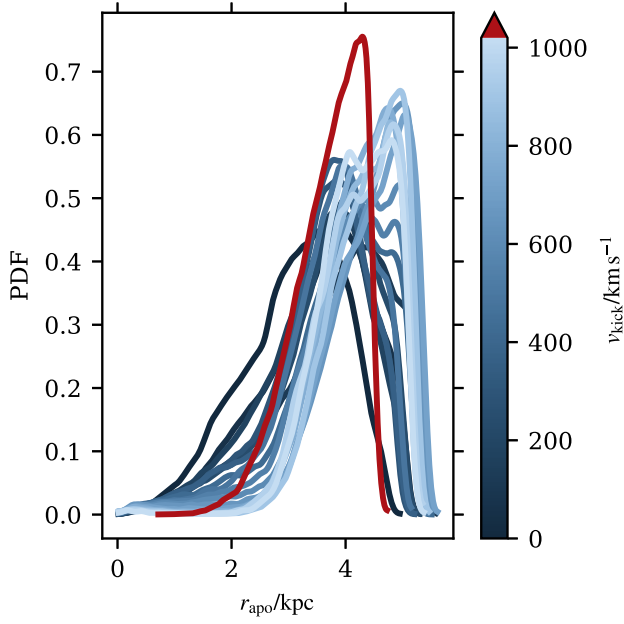


**Figure C1.** The distribution of apocentres for stellar orbits with a mean position within  $0.25r_{1/2}$  (matching the mock IFU maps), determined using the orbit analysis routine described in Section 5. All the distributions are left-skewed, where simulations with higher  $v_{\text{kick}}$  are more left-skewed than those with lower  $v_{\text{kick}}$ .

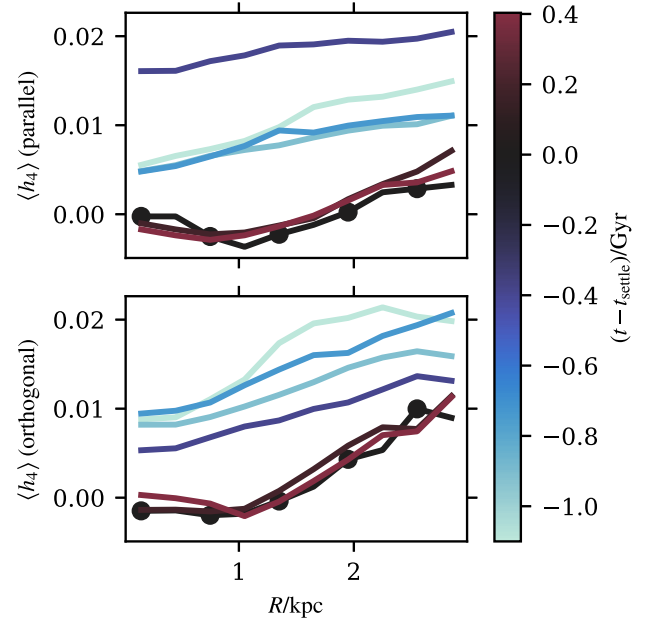


**Figure C2.** The dependence of the  $\langle h_4 \rangle$  profile on the time of analysis for a representative example  $v_{\text{kick}} = 900 \text{ km s}^{-1}$ . At early times, when the SMBH is still oscillating through the stellar medium, the  $\langle h_4 \rangle$  profile is overall elevated, and decreases as the SMBH begins to settle towards an equilibrium point. For times after the SMBH has settled (according to the definition presented in Section 3.2), the profiles are consistent in both the parallel and orthogonal projections of  $\langle h_4 \rangle$ . The profile corresponding to  $t - t_{\text{settle}} = 0 \text{ Gyr}$  is accentuated with circle markers.

This paper has been typeset from a  $\text{\TeX/L\TeX}$  file prepared by the author.